

BARC newsletter

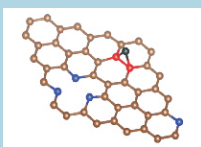
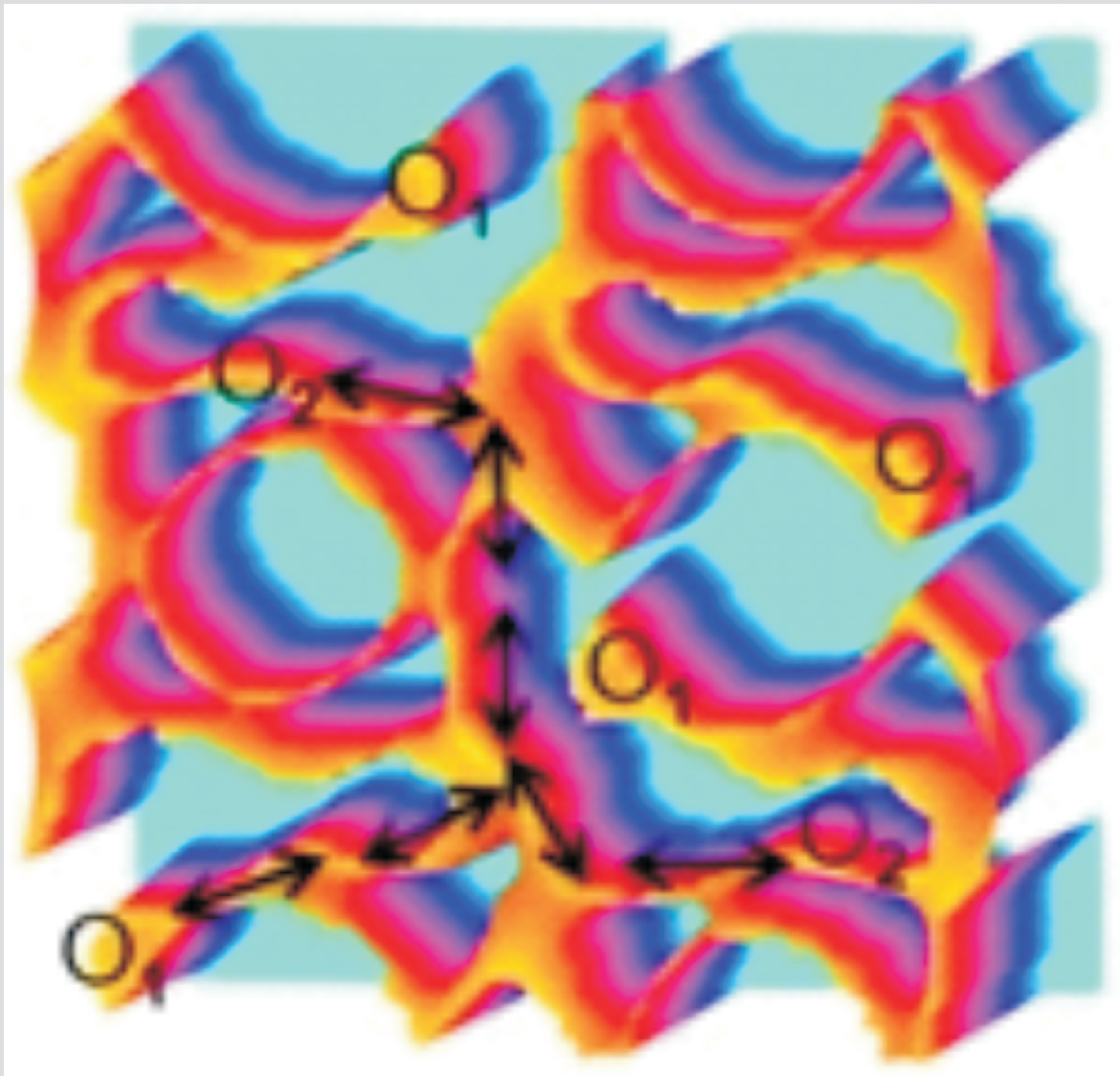
On Research in Physics

Volume 375 | May-June 2021 | ISSN:0976-2108

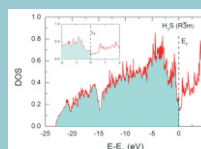
• Long-life Palladium thin film
H₂ sensor

• Thin film multilayers and their role
in condensed matter research

• Lithium Ion Batteries



Graphite
Defect topologies
and annihilation



H₃S
A new metallic phase
comes to fore



This page is intentionally left blank

BARC newsletter

Volume 375 | May-June 2021 | ISSN:0976-2108

On Research in Physics

5. **ASSOCIATE EDITORS' MESSAGE**

RESEARCH ARTICLES

7. **Defects in Highly Neutron Irradiated Graphite**

R. Mittal *et al*

12. **Present status and future potential of Lithium Ion Batteries**

K. Sandeep Rao *et al*

16. **Neutron Scattering of Novel Functional Magnetic Materials**

A.K. Bera *et al*

23. **Condensed matter research: Development of thin film multilayer Neutron and X-ray optics**

Arup Biswas *et al*

29. **Integrated Hydrogen gas sensing device based on sputter deposited Pd thin films**

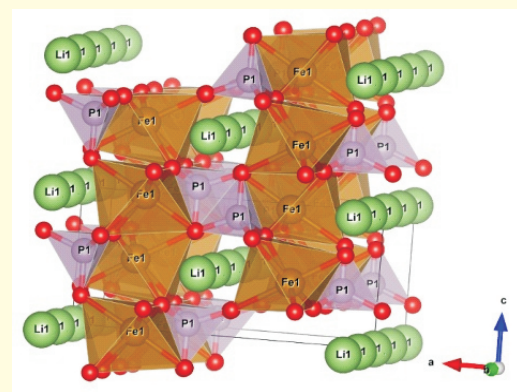
Niyanta Datta *et al*

34. **Structural Behaviour of Superconducting H_3S at Megabar Pressure**

P. Modak *et al*



Bird's eye view of Bhabha Atomic Research Centre Mumbai



Lithium ion channels of $LiFePO_4$



Pd thin film based Hydrogen gas sensor device

On the Cover

Continuous oxide ion conduction pathways in Lanthanum substituted yttrium iron garnets at 327 °C

@ BARC Photo

This page is intentionally left blank

associate editors' MESSAGE

Editorial Committee

Chairman

Dr. A.P. Tiwari
KMG

Editor

Dr. G. Ravi Kumar
SIRD

Members

Dr. A.K. Nayak, RED
Dr. G. Sugilal, PSDD
Dr. V.H. Patankar, ED
Dr. (Smt.) B.K. Sapra, RP&AD
Dr. L.M. Pant, NPD
Dr. Ranjan Mittal, SSPD
Dr. (Smt.) S. Mukhopadhyay, ChED
Dr. K.P. Muthe, TPD
Dr. V. Sudarsan, ChD
Dr. A.V.S.S.N. Rao, MBD
Dr. S.R. Shimjith, RCnD
Dr. Sandip Basu, RMC
Dr. Pranesh Sengupta, MSD
Dr. R. Tripathi, RCD

Member Secretary & Coordination

Madhav N, SIRD

Art, Design & Creative Work

Dinesh J. Vaidya, SIRD
Madhav N, SIRD



Bhabha Atomic Research Centre is an inter-disciplinary professional institute dedicated to stimulate accelerated growth of indigenous research and development. Recently there has been a tremendous growth in the area of materials science and engineering and their applications, and a wide variety of new materials have been developed with user specific properties.

It is a matter of pleasure for us to be associated with this issue of BARC Newsletter on the theme of materials. The present issue contains six articles based on a wide variety of research and development activities carried out in BARC. The articles include research work on neutron scattering of novel functional magnetic materials, lithium-ion batteries, defects in highly neutron irradiated graphite, and structural behaviour of superconducting H₃S at megabar pressure. Also included are articles on the developmental activities based on thin film multilayers for neutron and X-ray optics for condensed matter research and development of an integrated hydrogen-gas sensing device. We believe that these articles provide a glimpse of the techniques that are being currently being used for cutting edge materials research at BARC.

We express our sincere gratitude to all the scientists of BARC and HBNI who have contributed to the articles for this issue and to the reviewers who have spent time to make this issue possible.

(R. Mittal)

(K.P. Muthe)

This page is intentionally left blank

Defects in Highly Neutron Irradiated Graphite

*R. Mittal^{1,2}, M.K. Gupta¹, S.K. Mishra¹, S. Wajhal¹, H.K. Poswal³,
B.Singh^{1,2}, A.B. Shinde¹, P.S. Rama Krishna¹, Peram Delli Babu⁴,
Ratikant Mishra^{2,5}, Pulya Umamaheswara Sastry^{1,2}, Rakesh Ranjan⁶ and Samrath Lal Chaplot^{1,2}

¹Solid State Physics Division, Bhabha Atomic Research Centre, Mumbai, 400085, India

²Homi Bhabha National Institute, Anushaktinagar, Mumbai 400094

³High Pressure & Synchrotron Radiation Physics Division, Bhabha Atomic Research Centre, Trombay, Mumbai 400 085

⁴UGC-DAE Consortium for Scientific Research, Mumbai Centre, R5-Shed, BARC, Trombay, Mumbai - 400 085

⁵Chemistry Division, Bhabha Atomic Research Centre, Mumbai, 400085

⁶Reactor Operations Division, Bhabha Atomic Research Centre, Mumbai, 400085

Abstract

Graphite has been used as neutron moderator or reflector in many nuclear reactors. The irradiation of graphite in a nuclear reactor results in a complex population of defects. Heating of the irradiated graphite at high temperatures results in annihilation of the defects with release of an unusually large energy, called the Wigner energy. From various experiments on highly irradiated graphite samples from CIRUS reactor at Trombay and ab-initio simulations, we have for the first time identified various 2-, 3- and 4-coordinated topological structures in defected graphite, and provided microscopic mechanism of defect annihilation on heating and release of the Wigner energy. The annihilation process involves cascading cooperative movement of atoms in multiple steps involving an intermediate structure. Our work provides new insights in understanding of the defect topologies and annihilation in graphite which is of considerable importance to wider areas of graphitic materials including graphene and carbon nanotubes.

Keywords: Graphite, Neutron irradiation, Wigner energy, Ab-initio simulations, Annihilation of defects, Neutron diffraction

Introduction

Graphite has been used in high radiation environment, as neutron moderator or reflector, in many nuclear reactors, especially research and material testing reactors such as X-10 at Oak Ridge National Laboratory (USA), the Windscale Piles (UK) and G1 (Marcoule, France). About 250 kilo-tons of irradiated graphite inventory is present all over the world[1]. There is high interest in understanding of the change in behaviour of graphite, as well as in other graphitic materials such as graphene and carbon nanotubes due to irradiation[2,3]. The hexagonal structure of graphite[4] has layers of carbon atoms formed by strong covalent bonding in the a-b plane. These

layers are stacked along the hexagonal axis and are held by van der Waals forces. The irradiation of graphite in a nuclear reactor results in the knocking out of carbon atoms from their equilibrium sites. Defects in graphite are unusual since they involve very large potential energy and are prevented from annealing at ambient or moderately high temperatures due to a large energy barrier. Consequently, on heating of the irradiated graphite at high temperatures of around 200°C, the annealing of the defects is spontaneous with release of an unusually large energy, called the Wigner energy[5].

Extensive studies have been reported on unirradiated graphite, graphene and carbon nanotubes, including their highly

anisotropic elastic[6,7] and thermal-expansion behaviour[8] and spectroscopic studies[9,10] of the phonon spectrum. The macroscopic measurements on irradiated graphite reveal change in the thermal and elastic properties due to damage in the structure[5,11,12]. Neutron irradiation damage of graphite has been studied[13] by high-resolution transmission electron microscopy and Raman spectroscopy. First-principles theoretical studies of the structure, energies and behaviour of defects in graphitic materials has also been reported[14-17]. We note that there is no report of an experimental investigation of the structure of the defects at atomic-level, such as using neutron diffraction. So also, ab-initio simulations of the dynamical behavior of the knocked-out atoms, defect annealing mechanisms and the consequent Wigner energy release are not available. Here we address these aspects using a variety of experimental techniques and first-principles dynamical simulations.

Several graphite samples[18] irradiated with neutrons at various levels of fluence were taken out from a block of irradiated nuclear-grade graphite originally used in the reflector section of the CIRUS research reactor at Trombay, India. The highest fluence of the neutrons encountered by the samples is 2.6×10^{21} neutrons/cm² over a period of several decades. The neutron fluence seen by various samples is depicted in Fig. 1. We have also used an

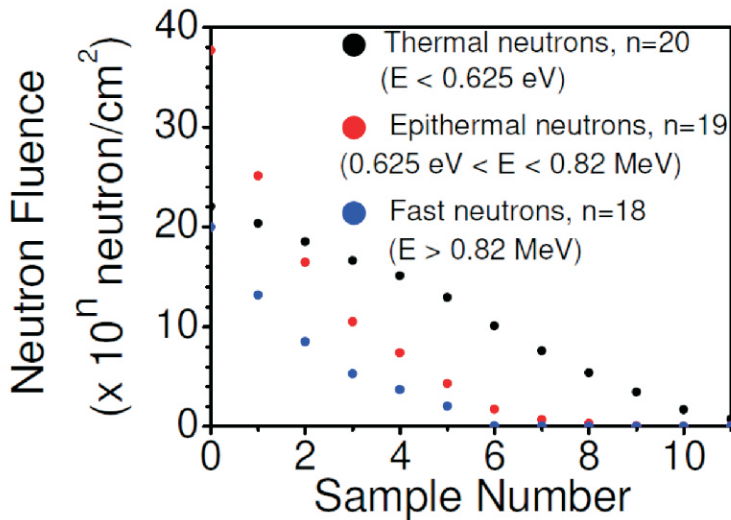


Fig. 1: Neutron fluence as seen by various graphite samples. The irradiated samples are numbered as S0 to S11 in the order of decreasing neutron fluence seen by them; i.e., S0 and S11 have seen the maximum and minimum neutron fluence, respectively. Another unirradiated sample for reference is assigned as sample number S12. The unit (10^n neutrons/cm²) of the vertical axis is different for thermal ($n=20$), epithermal ($n=19$) and fast neutrons($n=18$)[19] .

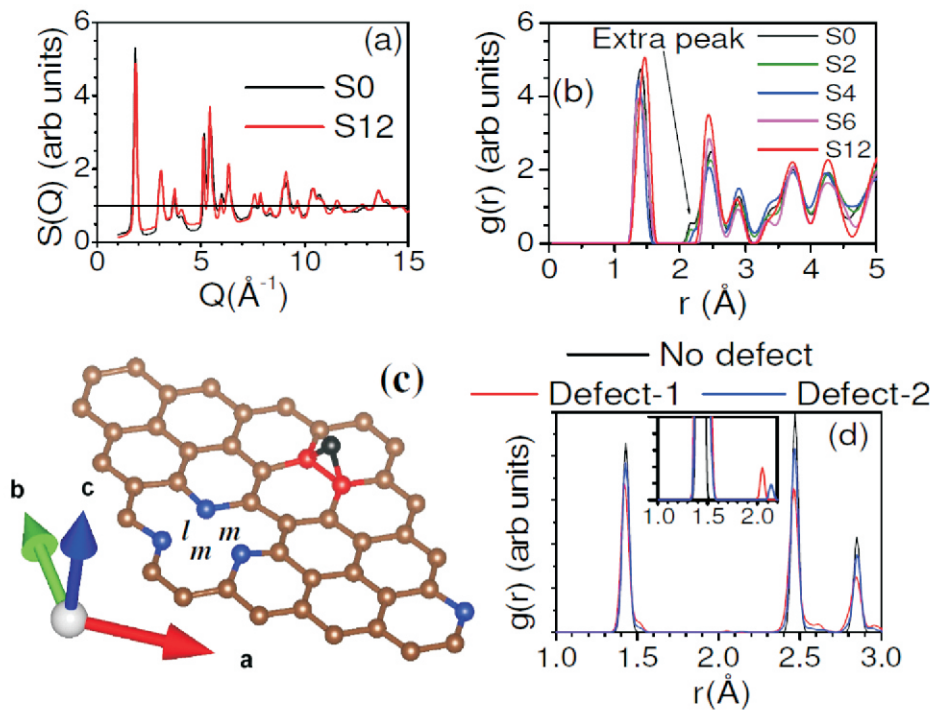


Fig. 2: Topological structures in defected graphite. (a) The neutron diffraction data ($S(Q)$ vs the neutron wave-vector transfer Q) for the un-irradiated (S12) and maximum irradiated (S0) samples. (b) The Pair distribution function of irradiated (S0, S2, S4, S6) and un-irradiated(S12) graphite as obtained from powder neutron diffraction data. (c) A graphite layer with a single Frankel defect in a $4 \times 4 \times 1$ super cell. “l” and “m” correspond to the interatomic distance of 2.06 Å to 2.66 Å respectively. The interstitial atom, and the 2-, 3- and 4-coordinated carbon atoms are shown by black, blue, brown and red colors, respectively. (d) The calculated pair correlation functions in the perfect and defected graphite structures. The labels Defect-1 and Defect-2 indicate the defect structures containing a single Frankel defect in $4 \times 4 \times 1$ and $4 \times 4 \times 2$ supercells, respectively. In the inset, a part of the figure is zoomed.[19] .

unirradiated sample for reference. The samples have been characterized by neutron and X-ray diffraction, differential scanning calorimetry, small angle X-ray scattering, Raman scattering and specific heat measurements, and the details are given in[19]. The results also show that the graphite samples which have been irradiated with very high neutron fluence of epithermal and fast neutrons (exceeding 10^{19} neutrons/cm²) are highly damaged, while the thermal neutron fluence is not so well correlated. To understand the experimental data on the structure and dynamics, we have performed ab-initio lattice dynamics and molecular dynamics simulations to model the defects, and to identify the mechanisms of annealing of defects in neutron irradiated graphite. While irradiation results in defects at various length scales, our studies have focussed on atomic level defects that are most relevant to the large Wigner energy release.

Topological structures in defected graphite

The experimental neutron diffraction data were obtained using the High-Q powder diffractometer at the Dhruva reactor, and are shown in Fig. 2a. It can be seen that peaks in the diffraction patterns of highly irradiated graphite are broader in comparison to that in the fresh sample. These data are analyzed to determine the real-space pair-distribution function, $g(r)$, which gives the probability of finding neighbors at a distance r . Fig.2b shows the pair distribution function for the unirradiated and several irradiated samples. It is evident from this figure that an additional peak in the $g(r)$ plot of the irradiated samples appears at $r=2.17$ Å with a redistribution of intensity in the $g(r)$ function. The neutron diffraction results can be understood using ab-initio simulation of the defect structure. As discussed below we find that this peak arises when an atom in the hexagonal layer is knocked-out resulting in a deformed pentagon. The peak at 2.17 Å results from one of the C-C distances in the deformed pentagon from where a vacancy has been created (Fig. 2c). The intensity of the peak at 2.17 Å gradually decreases with decrease of neutron fluence. This provides the experimental evidence for the defect and deformation in the hexagonal structure.

In order to study the defects in graphite we have performed simulation on a $4 \times 4 \times 1$

supercell (comprising two graphite layers and 64 atoms) of the graphite structure. Initially one of the carbon atoms in one of the graphite layers was moved in between the two layers, thus creating a vacancy-interstitial pair, also known as a Frenkel defect. The structural relaxation was performed for this configuration. The relaxed structure is shown in Fig. 2c. It can be seen that two of the carbon atoms in the hexagon below the interstitial carbon atom form four-fold coordination due to bonding with the interstitial atom ($C-C=1.40 \text{ \AA}$ to 1.52 \AA). The atom knocked out from a hexagon results in a deformed pentagon structure, in which one of the second neighbor distances of $C-C=2.45 \text{ \AA}$ (in the original hexagon) reduces to 2.06 \AA (in the deformed pentagon). Three of the carbon atoms now have 2-fold coordination. The defect structure thus consists of 2-, 3- and 4-coordinated carbon atoms. Further simulations on a larger $4 \times 4 \times 2$ (128 atoms) supercell confirmed similar defect structure.

We have plotted the pair correlation function (Fig. 2d) in the perfect and defect structures used in our calculations. We find that the configurations with 1 Frenkel defect in 64 atoms or 128 atoms give an additional peak at about 1.5 \AA , which corresponds to the four-fold coordinated carbon atoms. Further, in the $g(r)$ plot we find additional peaks at about 2.06 \AA and 2.15 \AA in the defect structure with 64 and 128 atoms respectively. As discussed above, these peaks correspond (Fig. 2c) to one of the second neighbor $C-C$ distances in a deformed pentagon as formed due to a vacancy of carbon atoms.

Phonon spectrum of defected graphite

The measured Raman spectra over $200-1800 \text{ cm}^{-1}$ from the fresh and maximum irradiated samples are shown in Fig. 3. It can be seen that the fresh sample shows an intense Raman mode at $\sim 1583 \text{ cm}^{-1}$ (G mode), and weak features at around 800 cm^{-1} , $\sim 1355 \text{ cm}^{-1}$ (D mode) and $\sim 1620 \text{ cm}^{-1}$ (D_2 mode). For the largest irradiated sample, the intensities of these weak features gain very significantly. The intensities of the broad low energy feather around 800 cm^{-1} and the D mode, and also the peak widths increase significantly for the samples irradiated with very high fluence of the epithermal and fast neutrons.

In order to understand the difference in the phonon spectrum at microscopic level we have calculated the phonon density of

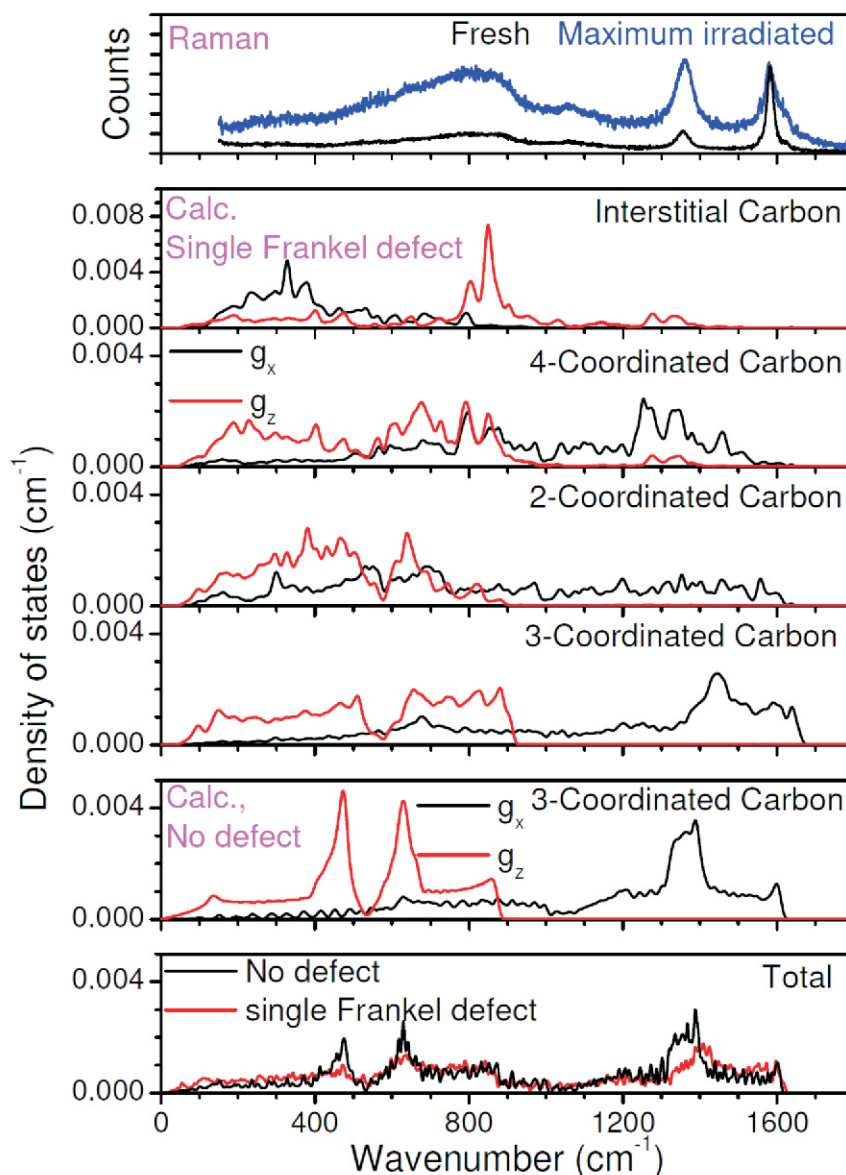


Fig. 3: The measured Raman spectra of the fresh and maximum irradiated graphite sample; and the calculated partial and total phonon density of states of graphite with a single Frankel defect in a $4 \times 4 \times 1$ supercell and with no defect. g_x and g_z are the x and z components of the partial phonon density of states respectively[19].

states as well as the in-plane and out-of-plane partial components of the phonon density of states in both the perfect and the defect structures. As discussed above, the defect structure with the $4 \times 4 \times 1$ supercell of graphite has 2-, 3- and 4- coordinated carbon atoms within a graphite layer as well as an interstitial atom in between two layers. We have calculated the partial density of states for each of these types of carbon atoms (Fig. 3).

The changes in the observed Raman spectra (Fig. 3) with irradiation can be understood in terms of the calculated partial phonon density of states of the 2-, 3- and 4- coordinated carbon atoms in the defect structure. We identify (Fig. 3) that

the most prominent increase in the intensity of the D-peak at 1360 cm^{-1} is due to the increase in the 4-coordinated carbon atoms. So also, the general increase of the intensity around 800 cm^{-1} may be ascribed to 2- and 3-coordinated carbon defects and the interstitial atom. The results are corroborated by simulations on a single Frankel defect in a $4 \times 4 \times 2$ super cell[19].

Annihilation of defects and release of Wigner energy

The recombination of interstitial atoms and vacancies is the key to the release of Wigner energy in graphite. Earlier calculations[14] showed the stored Wigner energy in a Frankel defect to be about

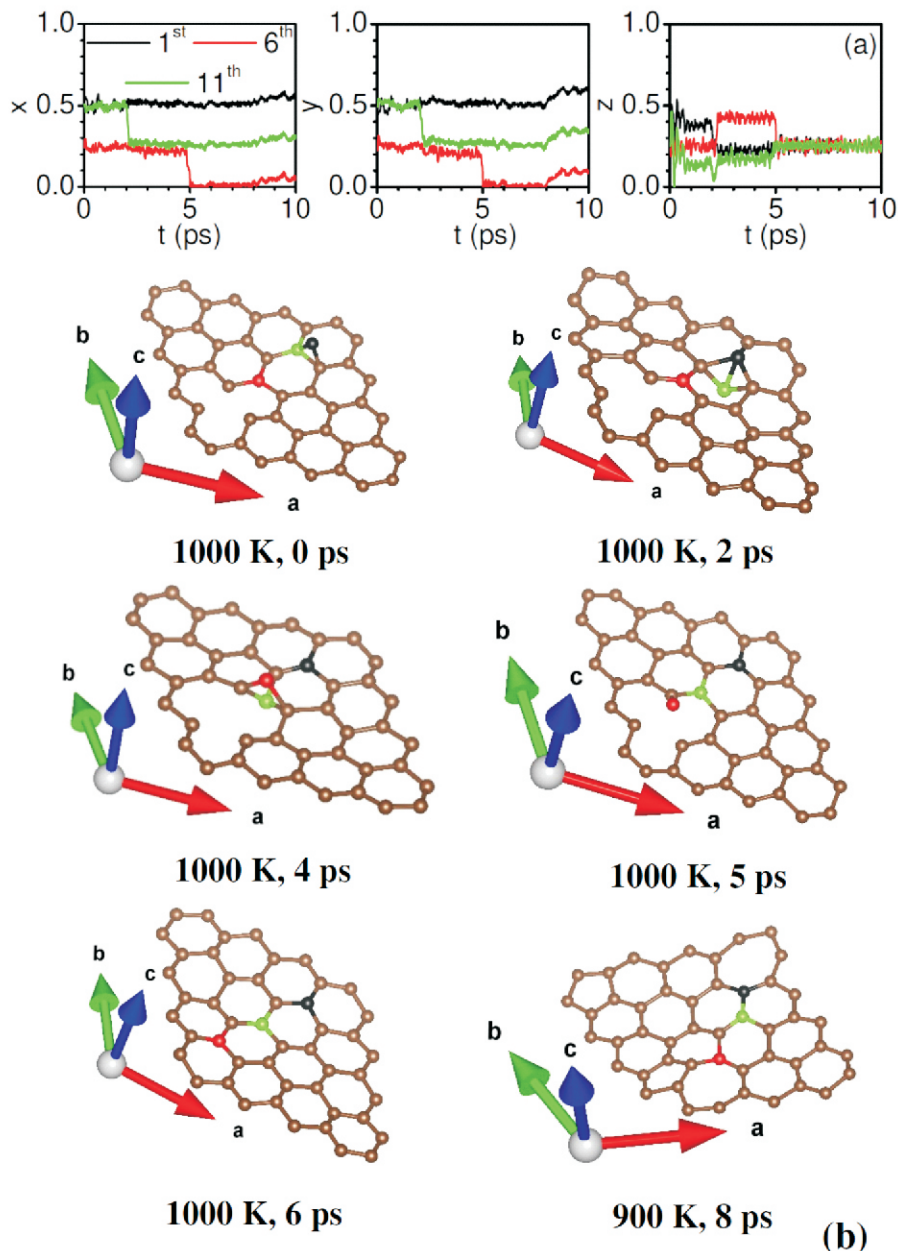


Fig. 4: Annihilation of defects in graphite. Results from ab-initio molecular dynamics simulations in a $4 \times 4 \times 1$ supercell with a single Frenkel defect at 1000 K.
 (a) The time dependence of fractional coordinates of selected three carbon atoms. x , y and z are the fractional coordinate along the a -, b - and c -axis respectively.
 (b) The snapshots of atoms in one layer of graphite. A snapshot of partially annealed defect at 900 K is also shown. The selected three carbon atoms are identified as 1st, 6th and 11th in (a) are shown in (b) by black, red and green circles respectively[19].

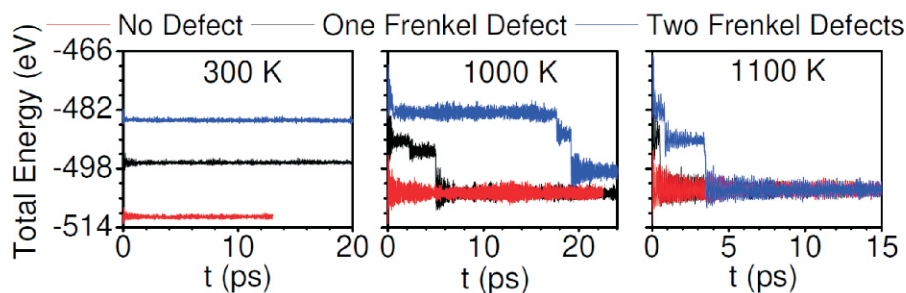


Fig. 5: Annihilation of defects and release of the Wigner energy. The total energy of $4 \times 4 \times 1$ supercell (64 atoms) as a function of time with a single and two Frenkel defects from ab-initio molecular dynamics simulations[19].

13-15 eV. The release of Wigner energy[5] in experiments is known to complete at about 650 K. We have verified this in our irradiated samples using Differential Scanning Calorimetry[19]. However our simulation which is performed at a small time-scale of ~ 200 ps, the temperature for the defect annihilation is expected to be overestimated. However, simulations are useful to understand the mechanism of annealing of defects in graphite.

The simulations are performed on the $4 \times 4 \times 1$ supercell with one Frenkel defect at several temperatures from 300 K to 1100 K. The atomic trajectories of carbon atoms have been monitored as a function of time up to 200 ps. Up to 800 K, the defect annihilation process did not start in 200 ps time. However, at 900 K within 7 ps the interstitial carbon atom moved into the graphite layer. At this time, the defect structure at 900 K (Fig. 4) consists of five- and seven-member carbon rings within the graphite layer. The structure did not relax further into hexagonal rings in the simulation up to 200 ps.

In the simulation at 1000 K, the defect energy is completely released in two steps as shown by the time dependence of the atomic coordinates. Fig. 4 shows snapshot of atoms at selected times. First at ~ 2.5 ps through a cooperative movement of neighboring carbon atoms we find that the interstitial carbon atom has moved closer to the vacancy. In the second step at ~ 5.5 ps, the hexagonal structure is restored. The simulations performed at 1100 K showed that within a short time of 1 ps the perfect hexagonal structure is formed. The cascading steps of cooperative movement of atoms represent the pathways of the defect annihilation process. (See Animations in[19], which provide visualization of likely different mechanisms of annealing of defects in multiple steps as discussed above).

We have calculated the total energy of the supercell as a function of time, which reveals the Wigner energy released during the defect annihilation process (Fig. 5). We find the Wigner energy at any temperature to be ~ 15 eV per vacancy-interstitial defect pair. However, a significant energy barrier prevents the annealing of the defect at a time-scale of 200 ps up to 800 K. However, at 900 K we found that, although the interstitial carbon atom moves in the graphite layer, the structure does not fully anneal in 200 ps time, and still retains a

potential energy of about 5 eV. At 1000 K, the energy of 15 eV is released during the defect annihilation in two steps (Fig. 5), while at 1100 K the same energy is released in a single step.

We have also performed the MD simulations with a structure consisting of two Frankel defects (Fig. 5) in the 4×4×1 supercell. In two Frankel defects the stored Wigner energy is calculated to be ~26.4 eV. We found that at 1000 K one Frankel defect has annealed at ~17.5 ps, while the second Frankel defect is not fully annealed until 100 ps as it forms a pair of five and seven-member rings. However, at 1100 K we found annealing of both the Frankel defects in 4 ps. The annihilation of the first Frankel defect releases about 10-11 eV of energy while that of the second Frankel defect releases about 15 eV. (See Animations in [19]).

Conclusions

In this paper, we have provided direct characterization of defects in neutron irradiated graphite through neutron diffraction, Raman scattering and specific heat measurements, and complemented the results by ab-initio simulations. Specifically, we have observed signatures of 2-, 3- and 4-coordinated carbon topologies around the Frankel defects in both the diffraction and Raman experiments. The microscopic understanding of annealing of defects on heating is achieved through ab-initio molecular dynamics simulations. These involve cooperative movement of atoms in several cascading steps depending on the distance between the vacancy and interstitial positions. The experimental and theoretical work has provided valuable insights in understanding of the structure and dynamical behavior of the defects in neutron irradiated graphite, the annihilation of the defects and consequently release of unusually large Wigner energy.

We note from our ab-initio simulations on various supercells that the defect structure in a graphite layer around a

Frankel defect is essentially independent of the separation of such defects along the hexagonal c-axis. This may be expected due to the much weaker van der Waals interaction between the graphite layers compared to the strong covalent bonding within the layers. Other graphitic materials including graphene and carbon nanotubes have similar two-dimensional structure and bonding as in a graphite layer, and these may also be used in high radiation environment including outer space. Therefore, the present work on highly irradiated graphite is of considerable importance to wider areas of graphitic materials.

Acknowledgments

The use of ANUPAM super-computing facility at BARC is acknowledged. SLC thanks the Indian National Science Academy for award of an INSA Senior Scientist position.

Corresponding Author*

Dr. R. Mittal (rmittal@barc.gov.in)

References

- [1] IAEA-TECDOC-1521, IAEA, Vienna (2006).
- [2] A. Krasheninnikov and F. Banhart, *Nature Materials* **6**, **723** (2007).
- [3] J. Lin, Z. Peng, Y. Liu, F. Ruiz-Zepeda, R. Ye, E. L. Samuel, M. J. Yacaman, B. I. Yakobson, and J. M. Tour, *Nature Communications* **5**, **1** (2014).
- [4] H. S. Lipson and A. Stokes, *Proceedings of the Royal Society of London. Series A. Mathematical and Physical Sciences* **181**, **101** (1942).
- [5] T. Iwata, *Journal of Nuclear Materials* **133**, **361** (1985).
- [6] P. De Andres, F. Guinea, and M. Katsnelson, *Physical Review B* **86**, **245409** (2012).
- [7] O. Blakslee, D. Proctor, E. Seldin, G. Spence, and T. Weng, *Journal of*

Applied Physics **41**, **3373** (1970).

- [8] B. Marsden, A. Mummery, and P. Mummery, *Proceedings of the Royal Society A: Mathematical, Physical and Engineering Sciences* **474**, 20180075 (2018).
- [9] P. Giura, N. Bonini, G. Creff, J. Brubach, P. Roy, and M. Lazzeri, *Physical Review B* **86**, 121404 (2012).
- [10] S. Rols, Z. Benes, E. Anglaret, J. Sauvajol, P. Papanek, J. Fischer, G. Coddens, H. Schober, and A. Dianoux, *Physical Review Letters* **85**, **5222** (2000).
- [11] E. Kaxiras and K. Pandey, *Physical Review Letters* **61**, **2693** (1988).
- [12] C. Ewels, R. Telling, A. El-Barbary, M. Heggie, and P. Briddon, *Physical Review Letters* **91**, **025505** (2003).
- [13] R. Krishna, A. Jones, L. McDermott, and B. Marsden, *Journal of Nuclear Materials* **467**, **557** (2015).
- [14] R. H. Telling, C. P. Ewels, A. Ahlam, and M. I. Heggie, *Nature materials* **2**, **333** (2003).
- [15] O. V. Yazyev, I. Tavernelli, U. Rothlisberger, and L. Helm, *Physical Review B* **75**, **115418** (2007).
- [16] I. Mosyagin, D. Gambino, D. G. Sangiovanni, I. A. Abrikosov, and N. M. Caffrey, *Physical Review B* **98**, **174103** (2018).
- [17] P. O. Lehtinen, A. S. Foster, Y. Ma, A. Krasheninnikov, and R. M. Nieminen, *Physical Review Letters* **93**, **187202** (2004).
- [18] R. Ranjan, S. Bhattacharya, P. V. Varde, C. G. Karhadkar, P. Mandal, M. K. Ojha, G. K. Mallik, and V. D. Alur, *BARC Report (External)* **BARC/2017/E/006**.
- [19] R. Mittal et al, *Physical Review B* **102**, **064103** (2020).

Present status and future potential of Lithium Ion Batteries

K. Sandeep Rao, Balaji P Mandal*, S. N. Achary, A. K. Tyagi

Chemistry Division, Bhabha Atomic Research Centre, Mumbai - 400085, India

Abstract

Lithium ion battery (LIB) is the most efficient energy storage device presently used in day to day activities. It consists of cathode, anode and electrolyte. A polymer separator is placed between the electrodes to avoid short circuit. The electrode materials must possess electronic as well as ionic conductivity whereas electrolyte is a purely ionic conductor. Electrode materials are being developed with the aim to increase the energy density, power density, cycling stability and safety of the cell. Among several cathodes $\text{Li}(\text{Ni}_x\text{Mn}_y\text{Co}_z)\text{O}_2$, $\text{Li}(\text{Ni}_x\text{Al}_y\text{Co}_z)\text{O}_2$, LiFePO_4 and among anodes carbon are being used in present day batteries.

Keywords: Lithium ion batteries, NMC333, LCO, LiFePO_4 (LFP), Graphitization of carbon

Introduction

Lithium ion batteries (LIB) are ubiquitous in most modern electronics ranging from electric-shavers to laptops. Lithium with its highest oxidation potential, low mass and high mobility, confers LIBs with high specific energy and power density. They also offer high cycle life, charge-discharge efficiency, as well as low capacity-fade. These factors combined with the relative earth abundance of LIB component elements, make it far superior to other battery chemistries like lead-acid and Nickel Metal Hydride (NiMH). Moreover, LIBs do not suffer from memory effect problem like Ni-Cd batteries and offer voltages nearly three times that of latter (Fig. 1). The self-discharge rate is also very low for LIBs (< 5% per month) as compared to Ni-Cd or Ni-MH batteries (~20-30% per month). Moreover, the global reserves of Li (~ 18 ppm of earth's crust) stand at ~ 43.6 Mt[1], sufficient for building ~12-14 billion electric vehicles (EVs), i.e. 10 times the current global number of automobiles. They have thus, become the focus of research from both industry and academia to meet the growing energy and power density requirements.

LIB Construction and working

A LIB is composed of a cathode (positive electrode) and an anode (negative

electrode), separated by an ion-conducting but electron blocking separator dipped in an electrolyte. The anode and cathode consist of electro-active material coated on metallic (Cu and Al respectively) current collector sheets that provide mechanical strength as well as a pathway for electron conduction to external circuit.

The first commercially successful LIB, introduced by Sony in 1991, (Fig. 2), utilized LiCoO_2 and carbon as cathode and anode, respectively. During charging cycle, electrons flow out of the Al current collector through external circuit towards anode. Meanwhile, Li^+ ions flow out into the electrolyte, traverse the ion permeable separator and intercalate between the graphene layers of carbon anode, where they are neutralized by the electrons entering from external circuit forming LiC_6 . The reverse process occurs during discharging process. It is this reversible to and fro shuttling of electrons and Li ions in the external and internal circuit respectively, that allows for storage/usage of electrical energy in a LIB.

Since Li is the most electropositive element (-3.04 V with respect to Standard Hydrogen Electrode), utilizing Li metal as anode would yield the highest cell voltage. Early attempts at this were foiled due to growth of lithium dendrites (tiny metallic

whiskers), upon deposition of Li^+ on anode during charging. These sharp dendrites eventually punctured the separator film and electrically shorted the cathode and anode, leading to a fire. This dendrite formation leading to battery fires was the major reason behind recall of Li/MoS_2 based batteries introduced in 1980s[2]. To overcome this issue, Li metal was replaced by carbon. In this case, the Li^+ ions are intercalated between the graphene layers of carbon.

Choice of electrode materials

a) Cathode Materials

For a material to be used as cathode in a LIB, it should have (i) low cost and be environment friendly (ii) high specific energy and power densities (iii) high Li^+ and electronic conductivity (iv) low structural and volume changes during charge/discharge cycles (v) chemical inertness towards electrolyte used in LIB (vi) electrode host structure tolerant to wide range of stoichiometry with respect to Li (vii) highly reversible lithiation/delithiation process in host structure (viii) high thermal stability. Moreover, the chemical potential of both cathode and anode must be well matched to the potential window (HOMO and LUMO) of electrolyte to allow large reversible capacity.

The cathodes for LIBs may be broadly classified as intercalation or conversion type depending on the basis how Li^+ are stored in them. In the former, Li^+ intercalates between inter-layer spacings in the host structure during discharging. Layered oxides (LiCoO_2), olivine (LiFePO_4), tavorite (LiFeSO_4F) and spinel (LiMn_2O_4) structures belong to this type, and they have a typical specific capacity in the range 100-200 mAh/g and typical voltage in the range 3 to 5V vs Li metal as anode. On the

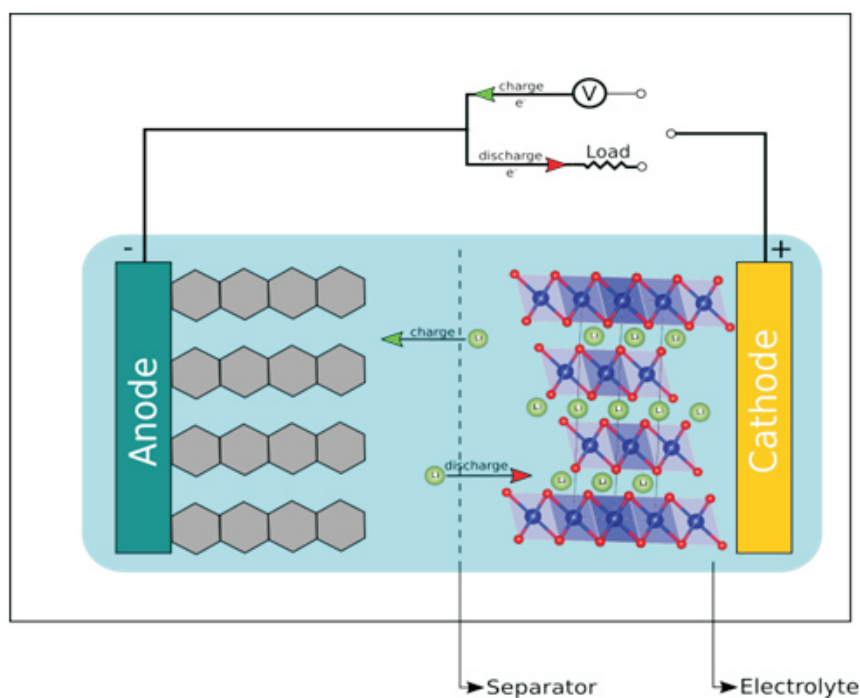


Fig. 1: Schematic of working of a typical intercalation type LIB

other hand, in conversion type, Li^+ ions displace the cation in the host cathode structure, leading to the formation of nano-precipitate of metallic cation during discharge.

The very first cathode that was developed for rechargeable LIBs was of the intercalation type, relying upon Li ion intercalation between layers of metal dichalcogenides (like TiS_2 and TaS_2). It was not commercially successful due to safety issues from Li metal anode but it paved the way for other layered materials.

The first commercially successful cathode material is LiCoO_2 [3](Fig. 3). It offers a higher voltage (3.5 – 4 V vs Li/Li^+) compared to the ~2V offered by LiTiS_2 and could be made in lithiated state enabling use of safer graphite anode. It possessed a high theoretical capacity (274 mAh/g), though only about half of it could be practically extracted in a reversible manner without structural changes. Its low thermal stability and specific capacity prompted research to replace Co with other transition metal ions. It was observed that certain metals provided certain desirable traits such as (i) increased thermal, cycling stability, lower cost (ii) prevention of cation migration to Li site (iii) increased capacity.

So, there was a move towards making binary/ternary oxides to get synergistic

effects. Among these materials, the most successful have been ternary (Ni/Mn/Co and Ni/Co/Al) oxides commonly referred as NMC and NCA, respectively. These oxides not only have similar/higher specific capacity compared to LCO but also achieve it at a lower cost due to reduced use of expensive Co. At the same time use Ni compensating for any capacity loss due to electro-chemically inactive Al/Mn ions.

b) $\text{Li}(\text{Ni}_x\text{Mn}_y\text{Co}_z)\text{O}_2$ ($x+y+z=1$)

Of the NMC oxide compositions developed, one of the first commercialized composition was NMC333: $\text{Li}(\text{Ni}_{0.3}\text{Mn}_{0.3}\text{Co}_{0.3})\text{O}_2$. Although NMC333 provides a reasonably high capacity (~150 mAh/g), it has a lower rate performance when compared to LCO.

It was observed that as the Ni content is increased in NMC, the specific capacity increases at the cost of thermal stability as well as rate performance due to Ni^{2+} ion's propensity for cation mixing. It even became the basis for categorization, with material containing >50% Ni classified as Ni-rich NMC. These Ni-rich materials suffer from low thermal stability as well as increased cation mixing leading to lower rate performance and high cell impedance[4]. The increased amount of Ni ions also correlates with increased amount of Ni^{4+} , with a low LUMO, which easily

oxidizes electrolyte speeding up cell degradation. To counter this issue, one strategy is to have core-shell particles, with a Ni-rich core contributing high specific capacity, and a Ni-poor shell that is more stable and does not oxidize electrolyte[5]. This approach was found to reduce electrolyte degradation but the difference in composition of core and shell led to differential volume changes during cycling.

c) $\text{Li}(\text{Ni}_x\text{Co}_y\text{Al}_z)\text{O}_2$ ($x+y+z=1$)

As discussed previously, Al can be used instead of Mn to provide enhanced thermal stability. The use of Al instead of heavier Mn yields higher specific capacity but slightly lower voltage vs Li metal. In contrast to NMC, only limited amount of Al(0.05-0.10) can be incorporated into NCA before the material begins to suffer from poor Li ion conductivity. Therefore, all practical compositions of NCA tend to Ni-rich and suffer from similar problems as Ni-rich NMC such as cation mixing, electrolyte oxidation etc. The most successful composition in NCA that is used in Tesla's EVs is $\text{LiNi}_{0.8}\text{Co}_{0.15}\text{Al}_{0.05}$.

d) LiFePO_4

One of the major safety concerns related to LIBs based on LCO and NMC is related to evolution of O_2 from the cathode with rising temperature. This evolved O_2 , then oxidizes electrolyte and other components in an exothermic fashion, and hence raise the temperature and even result in feedback loop that ends in a fire[6]. To mitigate this mechanism of catastrophic failure, it was proposed to use bulkier polyanions (XO_4)³⁻ ($\text{X}=\text{P}/\text{S}/\text{As}/\text{Sb}$) instead of O^{2-} in case of LCO. The rationale was that the stronger X-O bond would prevent the oxygen release failure mode seen in LCO. LiFePO_4 (LFP) was found to be the most promising with complete reversible exchange of Li ions in the 1-D channels of its olivine structure (see Fig. 3) as well as reasonable voltage of 3.5 V. LFP offers higher thermal stability, stable discharge potential as well as lower costs. The issue with LFP is its lower electronic and ionic conductivity compared to LCO and NMC. The poor conductivity is generally mitigated by synthesizing smaller nano-particles, applying a conductive carbon coating[7] as well as by cation doping. With these improvements, in spite of its lower energy density, it has found application in electric buses where safety and cost concerns outweigh volume/mass of cells.

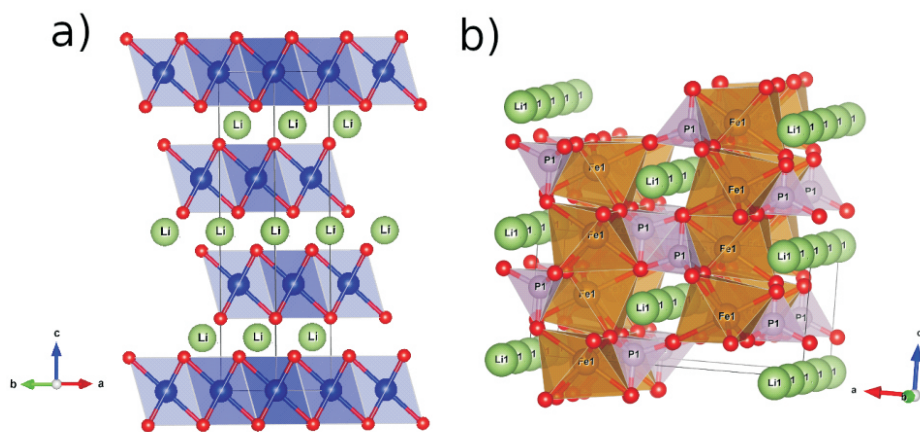


Fig. 2: (a) Layered structure of LiCoO_2 and (b) Li^+ channels of LiFePO_4

Anode Materials

To address the safety concerns posed by use of lithium metal as anode for lithium ion batteries, several alternate materials have been proposed. The alloying materials like Si-Li, Sn-Li suffered from low cycle life due to their large volume changes while Li-Al although stable under cycling exhibited very low rate capability as well as specific capacity.

i) Carbon

Due to the above mentioned drawbacks of alloying anodes, carbon has been considered and that quickly emerged as the most promising candidate due to its low lithiation/delithiation potential ($\sim 0.1 \text{ V}$ vs Li metal), good reversibility, high Li ion and electronic conductivity, low volume change during charging/discharging ($\sim 10\text{-}20\%$ strain), low cost and high availability. Li^+ ions are stored between two graphene planes, since one Li^+ can be stored per 6 carbon atoms, it has a theoretical capacity of 372 mAh/g . During the early days, when it was attempted to intercalate lithium into graphite, the propylene carbonate (PC) based electrolyte underwent decomposition. This decomposition layer was christened “Solid Electrolyte Interphase, SEI” and that separated the solid graphite electrode from the liquid electrolyte[9]. Moreover, PC molecules also intercalated between graphene layers leading to poor reversibility as well as loss of capacity as it exfoliates layers of graphene.

The Li^+ ion storage capacity was found to increase with increasing graphitization of carbon but it also decreased the stability of SEI. In more graphitic carbon, PC would

intercalate more and cause greater exfoliation. These findings in fact, prompted Yoshino et al [10] to choose coke-carbon, a less graphitic carbon that gave a moderately high capacity of $\sim 200 \text{ mAh/g}$ but with good reversibility and cycle stability for their patent of first secondary LIB. The co-intercalation of PC with Li^+ was subsequently solved by Fong et al. [11] using a mixture of PC along with ethylene carbonate (EC)[11]. They showed that electrolyte decomposition and SEI layer formation only occurs during the first few charging cycles and that the formed SEI layer persists during subsequent cycles with no capacity loss. Combinedly, these factors laid the foundation for graphite to become the most used anode material in commercial LIBs.

ii) $\text{Li}_4\text{Ti}_5\text{O}_{12}$

LTO possesses much better thermal stability, long cycle life and high rate capability due to its extremely efficient “zero-strain” ($\sim 0.2\%$ volume change) lithium insertion/extraction mechanism. It's higher lithiation/delithiation potential also prevents electrolyte decomposition at anode and eliminates loss of Li towards formation of a SEI layer (as opposed to carbon). Moreover, this high potential disfavors Li dendrite growth, even at high charge/discharge rates. This lack of SEI accords the high rate performance to this material and makes it a good choice for batteries requiring high power and large cycle-life but moderate energy capacity[13]. It was due to the above advantages that LTO was successfully commercialized despite its higher cost, higher lithiation/delithiation voltage $\sim 1.5 \text{ V}$ vs Li/Li^+ and lower capacity (175 mAh/g theoretical capacity).

Future Potential

a) Lithium-Sulphur and Lithium-Air

Lithium-Sulphur batteries are expected to succeed the current generation of lithium ion batteries due to several advantages of S such as (i) low cost and high availability (3% of earth's crust) (ii) it is environmentally benign (iii) it has high specific capacity (theoretical cap.: 1675 mAh/g) (iv) it has a lower operating voltage ($\sim 2 \text{ V}$) of Li-S compared to $\sim 3.7 \text{ V}$ for intercalation cathodes and can enhance cycle life due to reduction in possibility of electrolyte oxidation.

The theoretical capacity of Li-S batteries is expected to be five times of the current LIBs based on intercalation cathodes. The challenges that are being tackled towards practical utilization of these batteries are:

- Low electronic conductivity (10^{-31} S/cm) and large volume change ($\sim 80\%$) on cycling: This is being addressed by formulation of nanocomposites with enhanced conductivity and large void space.
- Low cycle life due to solubility of intermediate polysulphides (Li_2S_x) in the electrolyte leading to net loss of S content in electrode: electrolyte additives are being explored.

Lithium-air batteries mark another step forward in terms of specific capacity, with a theoretical capacity of 3840 mAh/g , i.e. 10 times more compared to current LIBs. They operate by reducing oxygen (from air) at cathode and oxidizing lithium at anode. This heterogeneous electrochemical coupling of gaseous O_2 and metallic Li in a safe, reversible and efficient manner is being pursued by researchers all over the world.

Conclusions

LIBs continue to be the dominant storage technology for high energy and power density applications. Advances towards practical implementation and Li-S and Li-air batteries are expected to keep up with growing demands for electric mobility applications. Safe, efficient and environmentally sustainable LIBs are expected to help reduce our carbon footprint and reduce dependence on polluting fossil fuels.

Corresponding Author*

Balaji P Mandal (bpmandal@barc.gov.in)

References

- [1] C. Grosjean, P. H. Miranda, M. Perrin, and P. Poggi, "Assessment of world lithium resources and consequences of their geographic distribution on the expected development of the electric vehicle industry," *Renew. Sustain. Energy Rev.*, 16, (2012) **1735–1744**.
- [2] K. Brandt, "Historical development of secondary lithium batteries," *Solid State Ion.*, 69, (1994) **173–183**.
- [3] K. Mizushima, P. C. Jones, P. J. Wiseman, and J. B. Goodenough, " Li_xCoO_2 (0," *Mater. Res. Bull.*, 15, (1980) **783–789**.
- [4] J. Oh et al., "High-rate cycling performance and surface analysis of $\text{LiNi}_{1-x}\text{Co}_{x/2}\text{Mn}_{x/2}\text{O}_2$ ($x=2/3, 0.4, 0.2$) cathode materials," *Mater. Chem. Phys.*, 222, (2019) **1–10**.
- [5] Z. Chen, Y. Qin, K. Amine, and Y.-K. Sun, "Role of surface coating on cathode materials for lithium-ion batteries," *J. Mater. Chem.*, 20, (2010) **7606–7612**.
- [6] K. Liu, Y. Liu, D. Lin, A. Pei, and Y. Cui, "Materials for lithium-ion battery safety," *Sci. Adv.*, 4, (2018) **9820**.
- [7] Z.-X. Chi, W. Zhang, F.-Q. Cheng, J.-T. Chen, A.-M. Cao, and L.-J. Wan, "Optimizing the carbon coating on LiFePO_4 for improved battery performance," *RSC Adv.*, 4, (2014) **7795–7798**.
- [8] A. N. Dey, "Electrochemical Alloying of Lithium in Organic Electrolytes," *J. Electrochem. Soc.*, 118, (1971). **10**.
- [9] E. Peled, "The Electrochemical Behavior of Alkali and Alkaline Earth Metals in Non aqueous Battery Systems—The Solid Electrolyte Interphase Model," *J. Electrochem. Soc.*, 126,(1979), **2047**.
- [10] A. Yoshino, K. Sanekika, and T. Nakajima, "Secondary battery," **US4668595A**, May 26, 1987.
- [11] R. Fong, U. von Sacken, and J. R. Dahn, "Studies of Lithium Intercalation into Carbons Using Non aqueous Electrochemical Cells," *J. Electrochem. Soc.*, 137, (1990) **2009**.
- [12] T. Ohzuku, A. Ueda, and N. Yamamoto, "Zero Strain Insertion Material of $\text{Li}[\text{Li}_{1/3}\text{Ti}_{5/3}]\text{O}_4$ for Rechargeable Lithium Cells," *J. Electrochem. Soc.*, 142,(1995) **1431**.
- [13] K. Zaghbi et al., "Safe and fast-charging Li-ion battery with long shelf life for power applications," *J. Power Sources*, 196, (2011) **3949–3954**.

Neutron Scattering of Novel Functional Magnetic Materials

A. K. Bera, A. Jain, A. Kumar, and S. M. Yusuf*

Solid State physics Division, Bhabha Atomic Research Centre, Mumbai 400085

Abstract

Advanced magnetic materials with improved functional magnetic properties are required for advances in technology and engineering. Microscopic understanding of the intertwined relation between the functionalities and structures (crystal/magnetic) of several functional magnetic materials is achieved by employing powerful neutron scattering technique. A glimpse of our recent results on some selective functional magnetic materials is presented here.

Keywords: Neutron scattering, antiferromagnets, spin chains, rare-earth manganites

Introduction

Novel functional magnetic materials are a group of material having interesting physical properties which are controlled/influenced by external applied magnetic field. These materials have applications in various fields ranging from data storage to medical investigations including drug delivery. Microscopic understanding of the relation between the structure (crystal/magnetic) and functionalities at the molecular and atomic scale is of paramount importance to advancing new technologies. The central point to achieve such microscopic understanding is the investigation of magnetic structure by neutron scattering [1]. In this article, we highlight recent developments in the study of functional magnetic materials in SSPD, BARC.

Investigation of low dimensional quantum magnets

Low-dimensional quantum magnets have received lots of attention in recent years as they represent tractable example of many body quantum systems. Low-dimensional magnetic systems refer to the system where the magnetic exchange interaction in one (two) directions is much higher compared with the values in the remaining two (one) directions. The reduction of dimensionality and small value of spin strongly enhance the quantum fluctuations in these compounds and lead to a range of exotic magnetic

phenomena. We have investigated such quantum phenomena in several naturally grown one- and two-dimensional magnetic materials [2-13].

Neutron scattering investigations of exotic quantum phases in a spin-1/2 metal-organic kagome compound

Among all geometrically frustrated networks, the $S = \frac{1}{2}$ nearest-neighbour Heisenberg antiferromagnet on the kagome lattice is a promising system where one can look for the novel quantum phenomena including the “resonating valence bond” state [14], gapped and gapless spin liquids as proposed theoretically for these systems. However, the experimental investigation of these systems is not easy because most of the kagome lattice antiferromagnets (AFMs) have either a large spin or a structural distortion. In our effort to investigate spin $\frac{1}{2}$ kagome lattice AFMs, we have synthesized a new compound with formula $\{[\text{Cu}_3(\text{CO}_3)_2(\text{bpe})_3] \cdot 2\text{ClO}_4\}_n$ (bpe=1,2-bis(4-pyridyl)ethane) [15], having ideal 2D kagome layers of Cu^{2+} ($3d^9$, $S=1/2$), in the crystallographic ab plane, with pillars of “bpe” ligands of length ~ 13.13 Å, separating the kagome layers [Fig. 1 (a)]. The $[\text{Cu}_3(\text{CO}_3)_2]^{2+}$ kagome layers in this compound are pillared by the bpe linkers along the c axis. The structural parameters for this compound make sure two-dimensionality of the kagome layers with a negligible inter-layer coupling.

The dc susceptibility [Fig. 1(b)] can be fit to a Curie-Weiss law at high temperatures ($T > 150$ K). The resulting Curie-Weiss temperature (θ_{CW}) of ~ -2.9 K implies an AFM exchange between the Cu^{2+} spins in the 2D kagome plane. In our neutron diffraction study [Fig. 1(c)], neither additional magnetic Bragg peaks nor an enhancement in the intensity of fundamental nuclear Bragg peaks has been observed down to 1.5 K, ruling out the presence of a long-range magnetic ordering (LRO). No depolarization of the neutron beam was observed down to 3 K, ruling out the presence of any ferromagnetic domains/clusters. Our Neutron diffraction and neutron depolarization measurements combined with the specific heat measurements [Fig. 1(b)] rule out the possibility of any LRO down to 86 mK. Our results suggest that strong quantum fluctuations enhanced by geometrical frustration suppress the long-range magnetic order and a spin-liquid like magnetic ground state is realized in this compound [2]. The derived phase diagram is shown in Fig.1 (d).

Magnetic correlations in the 2D honeycomb antiferromagnet $\text{Na}_2\text{Co}_2\text{TeO}_6$

In the quest for quantum spin liquids, the Kitaev honeycomb model is well known for its exact solvability and non-trivial properties that may be utilized in quantum computation. The model features bond-dependent **Ising interactions** (Kitaev interactions) between spin-1/2 degrees of freedom on a honeycomb lattice. Experimentally, the Kitaev honeycomb model has been realized only on 5d iridium and 4d ruthenium-based compounds [16,17]. Recently, it is proposed that the 3d Co^{2+} ions-based compounds can be also Kitaev materials [18]. Here, we report spin-spin correlations of the layered honeycomb compound $\text{Na}_2\text{Co}_2\text{TeO}_6$, a possible Kitaev material based on the 3d magnetic ion Co^{2+} . The magnetic layers consist of edge-

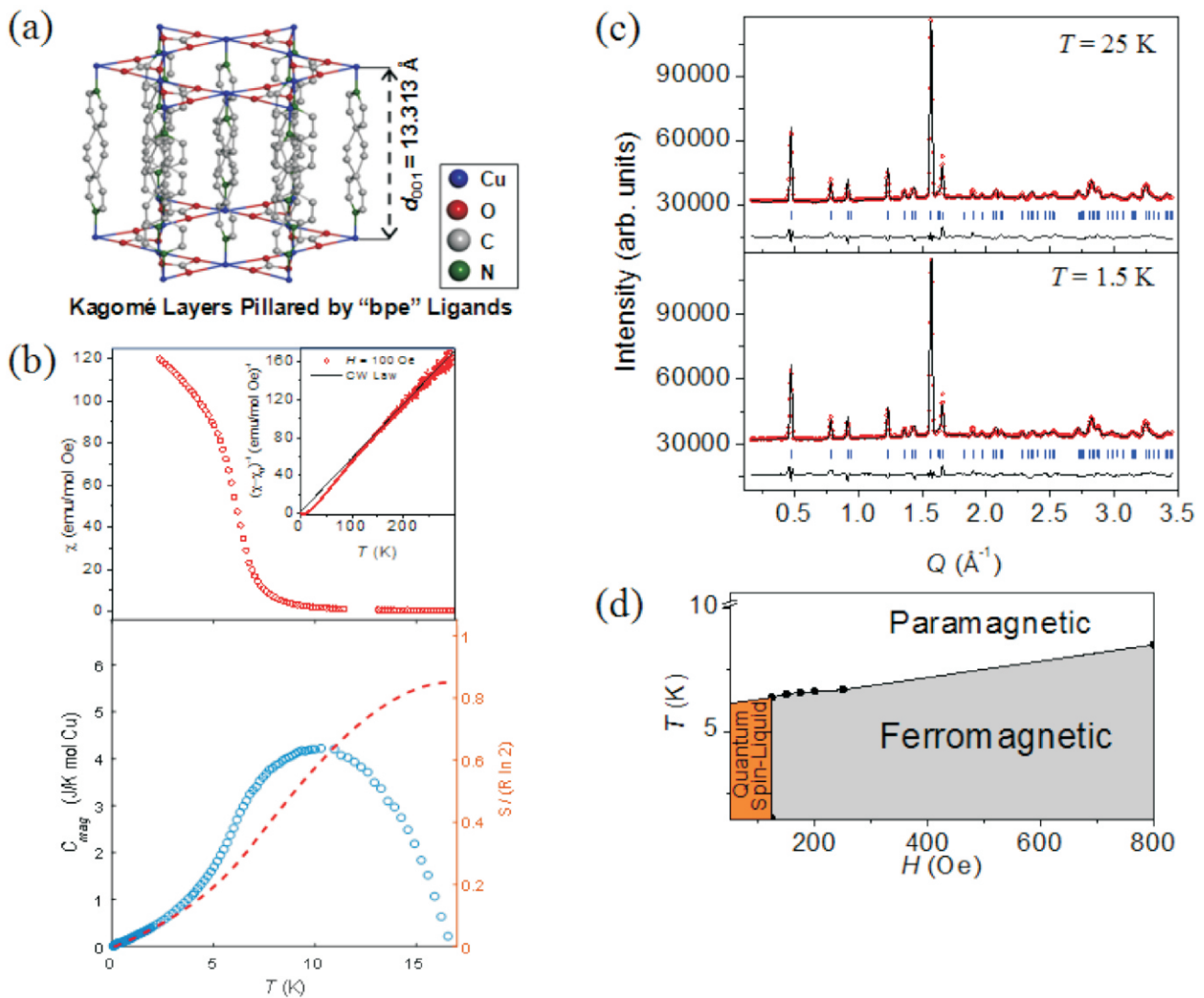


Fig. 1: (a) Crystal structure of the compound $\{[\text{Cu}_3(\text{CO}_3)_2(\text{bpe})_3]_2\text{ClO}_4\}_n$ (b) (top) temperature dependence of χ_{dc} measured with $H = 1000\text{e}$. Solid lines in the inset represent the Curie-Weiss (CW) fit. (bottom) Temperature dependence of the magnetic specific heat. The dashed line is the estimated magnetic entropy. (c) Observed (open circles) and calculated (solid lines) neutron diffraction patterns at 25 K and 1.5 K. (d) Magnetic phase diagram from neutron diffraction and thermodynamics measurements.

sharing CoO_6 and TeO_6 octahedra within the ab plane. The magnetic layers are well separated ($\sim 6 \text{ \AA}$) along the crystallographic c axis by the non-magnetic Na-layers providing a 2-dimensional magnetic system [Fig. 2]. The compound $\text{Na}_2\text{Co}_2\text{TeO}_6$ shows a zigzag AFM order below the $T_N = 25 \text{ K}$, due to the presence of an additional Heisenberg interaction (J) over the Kitaev interactions. The zigzag AFM state is proposed to be situated proximity to the quantum Kitaev spin-liquid state [3]. Our neutron powder diffraction study also reveals an anisotropic spin correlation in the ordered state, as evident from the different peak widths of the magnetic peaks $(000)+k$ and $(001)+k$ with $k = (0 \ 0 \ \frac{1}{2})$, with reduced order moments [Fig. 2]. Above the $T_N = 25 \text{ K}$, two-dimensional short-range spin-spin correlations have been found within the honeycomb planes [3].

Furthermore, our single crystal magnetization study reveals highly anisotropic magnetic behaviour and a suppression of the zigzag AFM order by an in-plane field of $\sim 6 \text{ T}$. Overall magnetic properties of $\text{Na}_2\text{Co}_2\text{TeO}_6$ manifest an intricate phase interplay that is generally expected near boundaries of competing phases, where quantum fluctuations are important.

Magnetic Hamiltonian of the spin-1 trimer chain compound $\text{CaNi}_3\text{P}_4\text{O}_{14}$

Low-dimensional magnetic materials, especially, one dimensional (1D) spin chains, are of current interest in condensed-matter physics as model experimental systems to study the physics of many-body quantum physics. Among them, the trimer spin chains are of particular interest due to the occurrence of

the magnetization plateaus, which can be viewed as an essentially macroscopic quantum phenomenon. At the magnetization plateau state magnetization is quantized to fractional values of the saturated magnetization value, analogous to the quantum Hall effect, proving a striking example of the macroscopic quantum phenomenon. We have investigated the spin-1 trimer chain compound $\text{CaNi}_3\text{P}_4\text{O}_{14}$ by elastic and inelastic neutron scattering. Experimental data reveal an AFM ordering below the $T_c = 16 \text{ K}$ and one-dimensional short-range spin correlations above the T_c [4]. Neutron inelastic data reveal gapped dispersive spin-wave excitations in the 3D long-range ordered magnetic state ($T_c = 16\text{K}$), and gapless magnetic excitations above the T_c due to the low-dimensional spin-spin correlations within chains [Fig. 3]. The

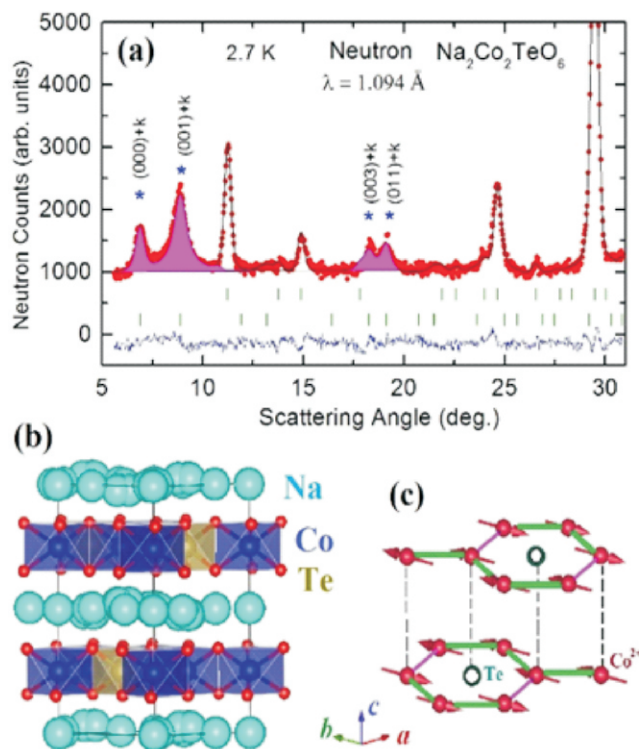


Fig. 2: (a) The Rietveld refined neutron diffraction pattern (shown a limited range for clarity) of $\text{Na}_2\text{Co}_2\text{TeO}_6$ measured at 2.7 K using the PD-1 diffractometer, Dhruva, BARC. The magnetic Bragg peaks are shown by the shaded regions. (b) and (c) The layered crystal and zigzag AFM magnetic structures of $\text{Na}_2\text{Co}_2\text{TeO}_6$, respectively.

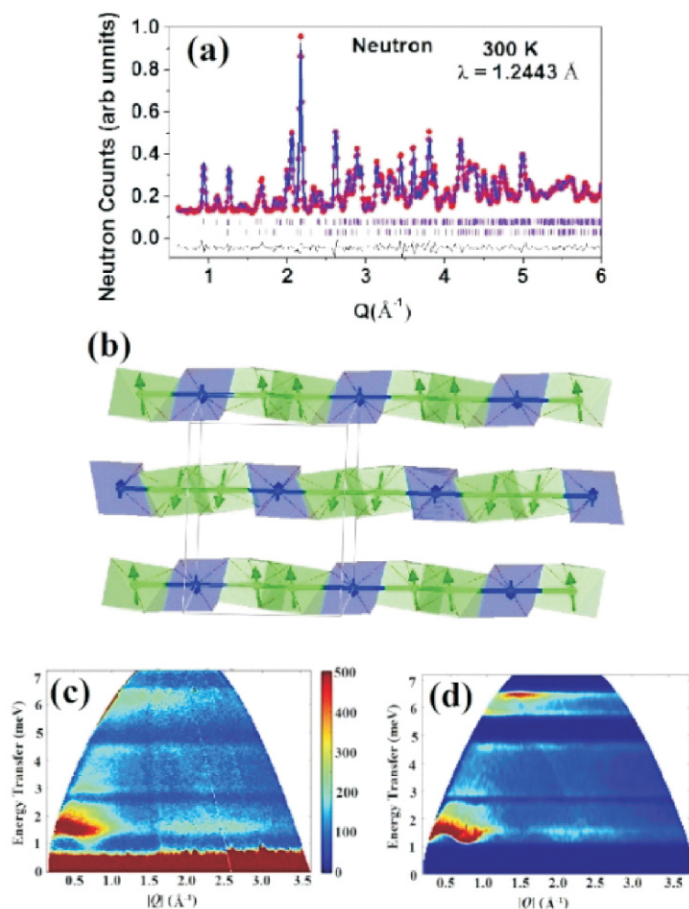


Fig. 3: (a) The Rietveld refined neutron diffraction pattern of $\text{CaNi}_3\text{P}_4\text{O}_{14}$ measured at 300 K using the PD-2 diffractometer, Dhruva, BARC. (b) The spin trimer crystal structure and spin arrangements below the $T_c=16$ K. (c) and (d) The experimentally measured and simulated (by spin wave theory) spin excitation spectra of $\text{CaNi}_3\text{P}_4\text{O}_{14}$.

magnetic Hamiltonian is determined by spin-wave theory analysis of the magnetic excitations, which reveals both ferromagnetic nearest neighbour J_1 and next-nearest neighbour J_2 interactions within the chains, and an antiferromagnetic interchain interaction J_3 . The strengths of the J_1 and J_2 are found to be closer ($J_2/J_1 = 0.81$), and J_3 is determined to be weaker ($|J_3/J_1| = 0.69$) with a weak single-ion anisotropy ($D/J = 0.19$) [5]. The strengths and signs of exchange interactions explain why the 1/3 magnetization is absent in the studied spin-1 compound $\text{CaNi}_3\text{P}_4\text{O}_{14}$ in contrast to its $S=5/2$ counterpart $\text{CaMn}_3\text{P}_4\text{O}_{14}$. Hence, the present study reveals the importance of full knowledge of the exchange interactions in trimer spin-chain compounds to understand their exotic magnetic properties, such as 1/3 magnetization plateau.

Study of phenomenon of magnetization reversal in functional oxides

Magnetization reversal or negative magnetization phenomenon was phenomenologically introduced in spinel ferrites by Néel in 1948 [19, 20]. This phenomenon mainly occurs due to dissimilar magnetization behaviours of two or more magnetic sublattices in materials. We have investigated this technologically important magnetization reversal phenomenon in spinels, garnets, and perovskite compounds by employing microscopic neutron diffraction technique [21-30]. We have given a first microscopic experimental explanation of the magnetization reversal phenomenon [24]. Subsequently, we have written a very first and comprehensive review on the subject covering all physics-related aspects of the phenomenon and its implications in magnetic memory, magneto-caloric and spin resolving devices [21]. Here we report investigations of magnetization reversal phenomenon in rare-earth based NdMnO_3 [22] and $\text{Ho}_3\text{Fe}_5\text{O}_{12}$ [29] magnetic oxides.

Rare-earth ordering driven spin reorientation and magnetization reversal in NdMnO_3

The perovskites are an important class of compounds that show multitude of physical properties such as spin dependent transport, multiferroic behavior, half metallic ferromagnetism, charge, and orbital ordering that are of great importance for various practical

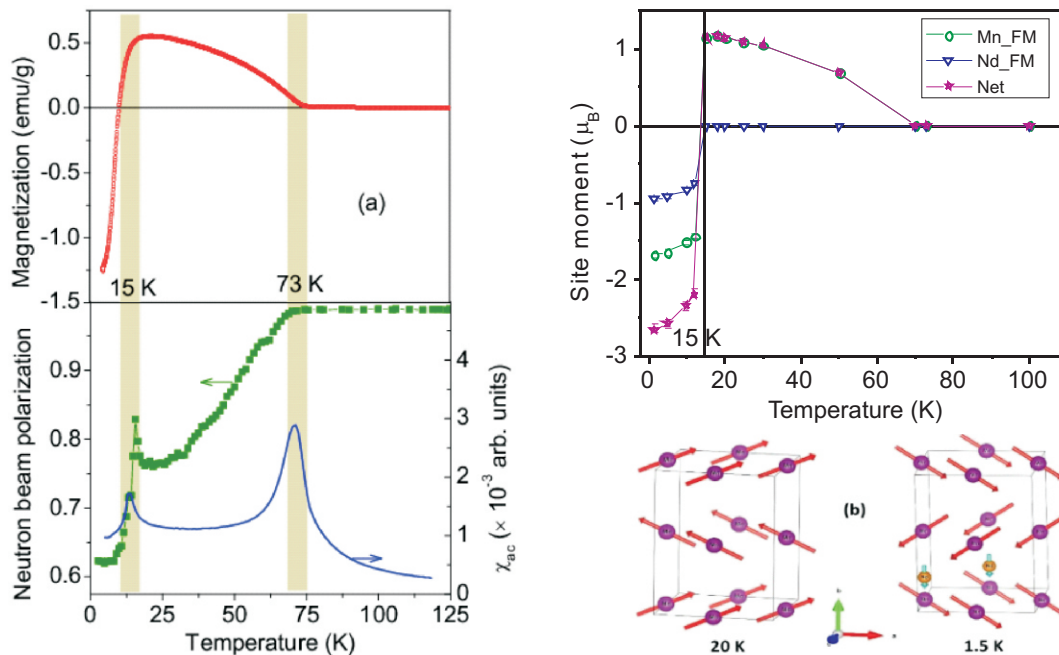


Fig. 4: (a) Magnetic ordering and magnetization reversal in NdMnO₃, shown by dc magnetization under 50 Oe, ac susceptibility (χ_{ac}) at 97 Hz, and neutron depolarization under 10 Oe field. (b) Microscopic understanding of Nd ordering induced Mn spin reorientation and magnetization reversal at 15 K by employing neutron diffraction.

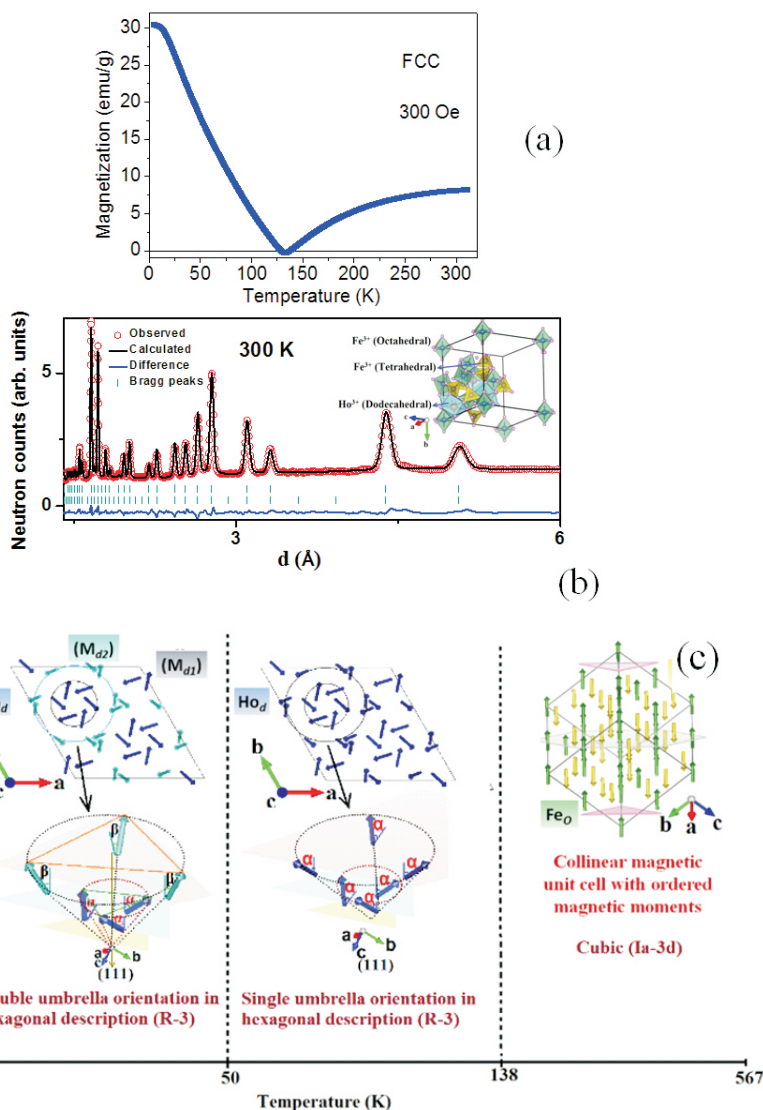


Fig. 5: (a) Magnetization compensation in Ho₂Fe₃O₇ (b) The Rietveld refined neutron diffraction pattern and the derived crystal structure (b) Schematic view of the magnetic unit cell for different temperature regions.

miniaturization and high stability. Here, we report the ionic conduction pathways and its temperature evolution [31-32], by neutron diffraction studies, in some of the magnetic materials that are also useful for the battery or solid oxide fuel cell (SOFC) applications.

Sodium conduction pathways in the layered battery material Na₂Ni₂TeO₆

Na₂Ni₂TeO₆ is layered battery material having Na as an active ion conductor. We have employed neutron diffraction to visualize Na-ion pathways and its temperature evolution in Na₂Ni₂TeO₆. By employing an advanced soft-bond-valence-sum analysis of the neutron diffraction patterns [Fig. 6 (a-b)], we experimentally demonstrate the visualization of microscopic sodium-ion conduction pathways [31] which reveal two-dimensional Na-ion conduction pathways that are confined within the *ab* planes of Na layers [Fig. 6(c-d)].

The experimentally derived pathways are excellent agreement with that recently reported theoretical results of molecular dynamics simulation. Our study further reveals that the layered crystal structure involving Na-ion layers is responsible for high ionic conductivity, and the local crystallographic environment of Na-ion sites is responsible for site-specific conductivity which has a strong temperature dependence [Fig. 6(c-d)].

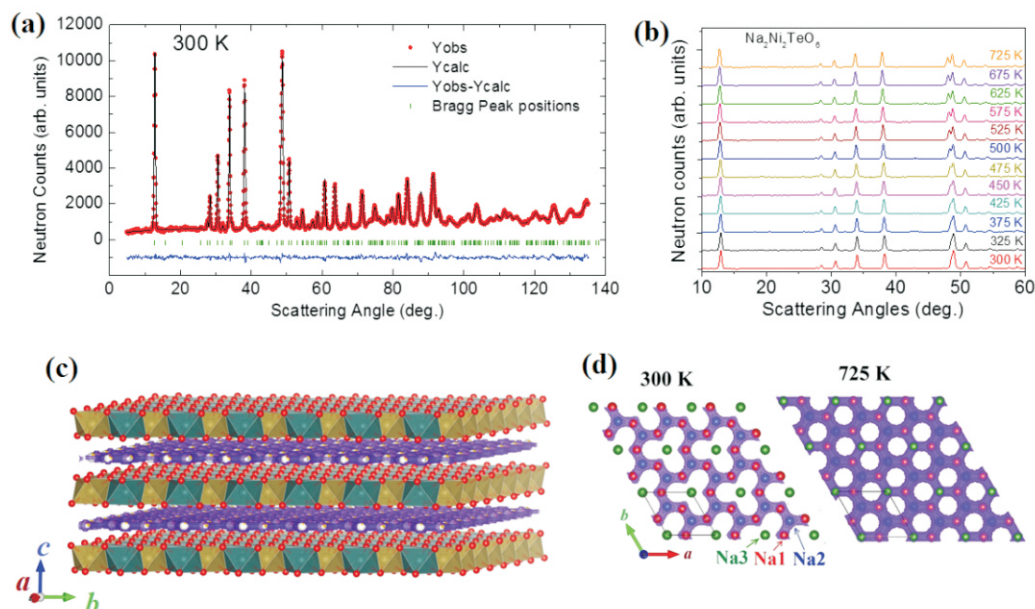


Fig. 6: (a) The Rietveld refined neutron diffraction pattern, measured at 300 K using the PD-2 diffractometer, Dhruva, BARC, for the layered Na-ion battery material $\text{Na}_2\text{Ni}_2\text{TeO}_6$ (b) The temperature dependent neutron diffraction patterns over the temperature range between 300 and 725 K (c) The two-dimensional Na-conduction pathways in the crystal lattice (d) The in-plane view of the Na-ion conduction pathways at 300 and 725 K.

applications. However, the role of rare-earth (R) moment ordering, that introduces finite and anisotropic f - d exchange interactions, in controlling technologically important properties of rare-earth manganites ($RMnO_3$) compounds, is not investigated in great details. In our neutron diffraction study on NdMnO_3 , for the first time, we have observed a strong evidence of rare-earth moment ordering driven Mn spin-reorientation transition in a larger R (Nd) ion based $RMnO_3$ compound. In particular, we show that Nd moment ordering at 15 K derives a Mn spin-reorientation and a concurrent structural distortion in NdMnO_3 compound. Our study also provides a microscopic understanding of the observed magnetic reversal phenomenon (in a field cooled dc magnetization study) [22] at the Nd moment ordering in NdMnO_3 compound.

By employing neutron diffraction, neutron depolarization, dc magnetization and ac susceptibility techniques [Fig. 4(a)], we have revealed a canted antiferromagnetic type spin arrangement (with a net FM component along b axis) for the Mn sublattice in the temperature range of 73 – 15 K. We have also established the ordering of Nd sublattice below 15 K in this compound. For the first time, we have shown that the ordering of the Nd sublattice drives a reorientation (by 180°) of the net FM moment of the Mn sublattice along the b -axis [Fig. 4 (b)]. Such a Mn spin reorientation explains the magnetization reversal phenomenon present in this

perovskite compound [22]. This new finding is significant considering the fact that the $RMnO_3$ compounds with smaller R ions (R : Ho, Er, Yb) show a Mn spin reorientation at rare-earth ordering and depict stronger coupling of the magneto-electric, magneto-elastic, and thermoelectric properties. Our finding, viz. occurrence of Mn spin reorientation in a larger ion (Nd) manganite, should encourage a reinvestigation of the $RMnO_3$ compounds with larger R ions for possible correlations among spin reorientation and magneto-caloric, thermoelectric, dielectric, ferroelectric properties of the $RMnO_3$ compounds.

Magnetization compensation phenomenon and its correlations in $\text{Ho}_3\text{Fe}_5\text{O}_{12}$

The ferrite garnet system, $\text{Ho}_3\text{Fe}_5\text{O}_{12}$ with Fe-Octahedral (Fe_o), Fe-Tetrahedral (Fe_t), and Ho-dodecahedral (Ho_d) magnetic sublattices is another system that exhibits magnetization compensation phenomenon at 138 K (T_{COMP}) [29] as shown in Fig. 5(a). The system exhibits magnetic ordering at 567 K and another magnetic transition at lower temperature (~ 50 K). Macroscopic, mesoscopic, and microscopic understanding of magnetization compensation and magnetic transition at ~ 50 K is studied by dc magnetization, neutron depolarization, and neutron diffraction techniques, respectively. $\text{Ho}_3\text{Fe}_5\text{O}_{12}$ system shows a sign reversal of magnetization below the T_{COMP} under low

(~ 50 Oe) applied magnetic field. Neutron depolarization study infers a zero-domain magnetization state at T_{COMP} with a full recovery of transmitted neutron beam polarization; this confirms the spin compensation at 138 K. Room temperature Rietveld refined neutron diffraction pattern with derived cubic crystal structure is shown in the Fig. 5(b). Our neutron diffraction study has revealed a ferrimagnetic ordering of FeO and FeT sublattices and Hods sublattice ordering takes place below the T_{COMP} into a single umbrella type canted spin configuration. This results in reduction of unit cell symmetry from cubic (1a-3d) to rhombohedral (R-3) [29]. Further below 50 K, Ho^{3+} sites split into two inequivalent magnetic sublattices, having different moments and canting angles, and leading to a double umbrella type magnetic structure as shown in Fig. 5(c).

Ionic conduction pathways in the superionic conductors for SOFC and battery applications

Superionic conductors are an important group of materials that have large-scale technological applications in the areas of energy storage and generation (electrolyzers, batteries, and fuel cells), gas sensors, and electrochromic devices. Such conductors are essential for the development of all-solid-state electrochemical devices, which have many advantages over those based on liquid electrolytes including ease of

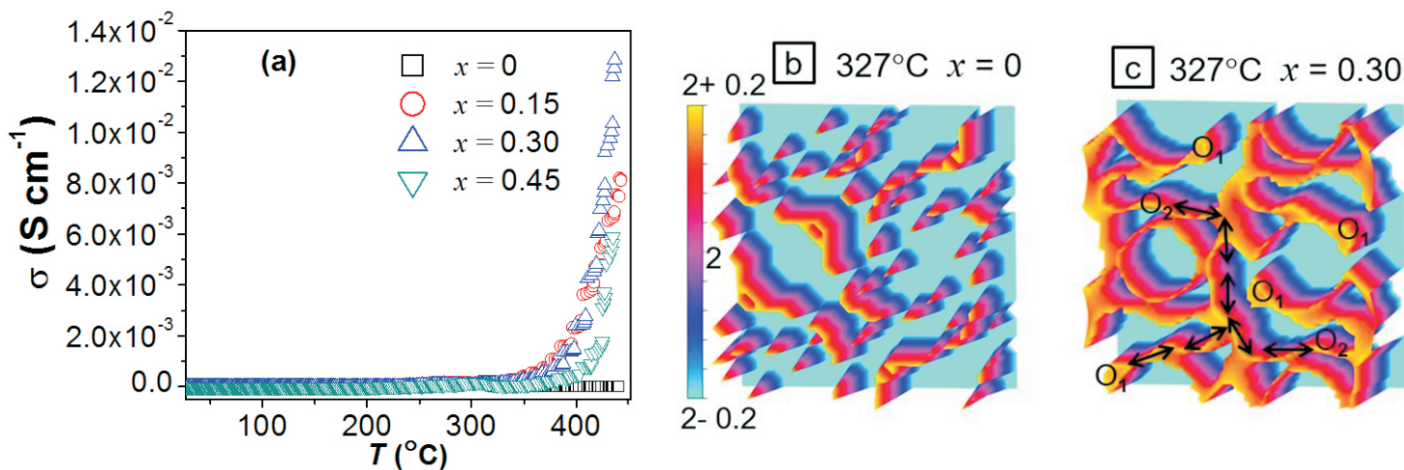


Fig. 7: (a) Temperature variations of ionic conductivities (σ) of $\text{La}_x\text{Y}_{3-x}\text{Fe}_5\text{O}_{12+\delta}$ ($x = 0, 0.15, 0.30$, and 0.45) compounds (b) Discontinuous and (c) continuous oxide ion conduction pathways in (100) plane at 327 °C in the parent ($x = 0$) and La substituted ($x = 0.3$) compounds, respectively.

Neutron investigations of oxide ion conduction pathways in $\text{La}_x\text{Y}_{3-x}\text{Fe}_5\text{O}_{12+\delta}$ garnets

In another study on the La substituted yttrium iron garnets $\text{La}_x\text{Y}_{3-x}\text{Fe}_5\text{O}_{12+\delta}$ ($x = 0 - 0.45$), we address the issue of achieving high oxide ion conductivity [Fig. 7 (a)] at low temperatures (< 500 °C) in stable electrolytes for SOFC technology [32]. The oxide ion conduction pathways have been derived from neutron diffraction data by the soft-bond-valence-sum analysis. We reveal that the oxide ion conduction is based on an excess oxide ion concentration in the garnets and a judicious substitution of high electropositive La^{3+} ions ($x = 0.45$) affords continuous and easy oxide ion conduction pathways through polyhedral networks even at a low temperature of 327°C which are absent in the parent $x=0$ compound [Figs. 7 (b) and (c)]. The observed high oxide-ion conductivity at low temperatures in the present trivalent substituted garnets is a remarkable finding for the development of an efficient SOFC technology.

Summary

In summary, we have presented here structural and magnetic properties of novel functional magnetic materials, investigated by microscopic neutron scattering and other thermodynamic measurements. Microscopic understanding of the relation between the structure and magnetic properties has been obtained using the neutron scattering technique. In some cases, understanding of the relation between the structure (crystal/magnetic) and functionalities at the molecular and

atomic scales has been obtained. The fundamental understanding obtained through neutron scattering study is useful for predictive design of functional materials for memory, energy, and sensors applications of advanced magnetic materials.

Acknowledgment

Authors respectfully acknowledge the contributions of their collaborators in the work reported in this article.

Corresponding Author*

S. M. Yusuf (smyusuf@barc.gov.in)

References

- [1] S. M. Yusuf and A. Kumar, *Appl. Phys. Rev.* **4**, **031303** (2017).
- [2] A. Jain, S. M. Yusuf, P. Kanoo, S. K. Dhar, and T. K. Maji, *Phys. Rev. B (rapid)* **101**, **140** (2020).
- [3] A. K. Bera, S. M. Yusuf, A. Kumar, and C. Ritter, *Phys. Rev. B* **95**, **094424** (2017).
- [4] A. K. Bera, S. M. Yusuf, A. Kumar, M. Majumder, K. Ghoshray and L. Keller, *Phys. Rev. B* **93**, **184409** (2016).
- [5] A. K. Bera, S. M. Yusuf and D. T. Adroja, *Phys. Rev. B* **97**, **224413** (2018).
- [6] A. Yogi, A. K. Bera, A. Mohan, R. Kulkarni, S. M. Yusuf, A. Hoser, A. A. Tsirlin, M. Isobe, and A. Thamizhavel, *Inorg. Chem. Frontiers* **6**, **2736-2746** (2019).
- [7] A. Yogi, A. K. Bera, A. Maurya, R.

Kulkarni, S. M. Yusuf, A. Hoser, A. A. Tsirlin, and A. Thamizhavel, *Phys. Rev. B* **95**, **024401** (2017).

- [8] P. Suresh, K. Vijaya Laxmi, A. K. Bera, S. M. Yusuf, B. Lingam Chittari, J. Jung and P. S. Anil Kumar, *Phys. Rev. B* **97**, **184419** (2018).
- [9] A. Singh, A. Jain, A. Ray, B. Padmanabhan, R. Yadav, V. Nassif, S. Husain, S. M. Yusuf, T. Maitra, V. K. Malik, *Phys. Rev. B* **96**, **144420** (2017).
- [10] R. Shukla, A. Jain, M. Miryala, M. Murakami, K. Ueno, S. M. Yusuf, R. S. Dhaka *J. Phys. Chem. C* **123**, **22457** (2019).
- [11] A. Singh, S. Rajput, P. Balasubramanian, M. Anas, F. Damay, C. M. N. Kumar, G. Eguchi, A. Jain, S. M. Yusuf, T. Maitra, and V. K. Malik, *Phys. Rev. B* **102**, **144432** (2020).
- [12] S. S. Islam, Vikram Singh, K. Somesh, Prashanta K. Mukharjee, A. Jain, S. M. Yusuf, and R. Nath, *Phys. Rev. B* **102**, **134433** (2020).
- [13] K. K. Kumawat, A. Jain, S. S. Meena, and S. M. Yusuf, *J. Alloy. Compd.*, **865**, **158849** (2021).
- [14] P. W. Anderson, *Science* **235**, **1196** (1987).
- [15] P. Kanoo, C. Madhu, G. Mostafa, T. K. Maji, A. Sundaresan, S. K. Pati and C. N. R. Rao, *Dalton Trans.* **5062-5064** (2009).
- [16] S. H. Chun, et al., *Nat. Phys.* **11**, **462** (2015).

- [17] A. Banerjee et al., Nat. Mat. 15, **733** (2016).
- [18] H Liu and G. Khaliullin, Phys. Rev. B 97, **014407** (2018).
- [19] L. Neel, Ann. Phys. (Paris) 3, **137** (1948)
- [20] T. Nagata, Rock Magnetism, second ed., Maruzen, Tokyo, 1961.
- [21] A. Kumar and S.M. Yusuf, Phys. Rep. 556, **1** (2015).
- [22] A. Kumar, S. M. Yusuf, and C. Ritter, Phys. Rev. B 96, **014427** (2017).
- [23] A. Kumar, S. M. Yusuf, J. Appl. Phys. 121, **223903** (2017).
- [24] A. Kumar, S. M. Yusuf, L. Keller, JV Yakhmi, Phys. Rev. Lett. 101, **207206** (2008).
- [25] A. Kumar and S. M. Yusuf, Physica B 551, **104** (2018).
- [26] M.Ghanathe, A. Kumar, and S. M. Yusuf, J. Appl. Phys. 125, **093903** (2019).
- [27] Deepak, A. Kumar, and S.M. Yusuf, J. App. Phys. 127, **213903** (2020).
- [28] M. Y. Yang, S.Seong, E. Lee, M.Ghanathe, A. Kumar, S. M. Yusuf, Y. Kim, J. S. Kang Appl. Phys. Lett. 116, **252401** (2020).
- [29] M. Ghanathe, A. Kumar, I. da Silva, and S. M. Yusuf, J. Magn. Magn. Mater. 523, **167632** (2021).
- [30] A. Kumar, S. K. Giri, T. K. Nath, C. Ritter, S. M. Yusuf, J. Appl. Phys. 128, **203901** (2020).
- [31] A. K. Bera and S. M. Yusuf, J. Phys. Chem. C, 124, **4421** (2020).
- [32] D. R. Bhosale, S. M. Yusuf, A. Kumar, M. D.Mukadam, S. I. Patil, Phys. Rev. Mater. 1, **015001** (2017).

Condensed matter research

Development of thin film multilayer Neutron and X-ray optics

Arup Biswas, Piyali Sarkar Roy, Abharana N and Dibyendu Bhattacharyya*

Atomic & Molecular Physics Division, Bhabha Atomic Research Centre, Mumbai – 400 085

Abstract

Over the last few years, a comprehensive facility has been developed at A&MPD, BARC for development of large area thin film multilayer devices for application in synchrotron and neutron based experiments for condensed matter research. This includes a 9 m long in-house developed in-line magnetron sputtering system and a state-of-art dual ion beam sputtering system. The devices being fabricated regularly in these systems include long strip-type synchrotron mirrors, multilayer X-ray mirrors, neutron supermirrors and supermirror polarisers. The performance of these devices are found to be comparable with international standards and these devices are employed in real applications in neutron and synchrotron facilities.

Keywords: DC Magnetron Sputtering, Ion Beam Sputtering, Thin film, Multilayer, X-ray mirror, Neutron Supermirror

Introduction

In condensed matter research neutron and X-ray are being extensively used as probes for understanding various physical properties of materials. Recently these have been boosted worldwide by the availability of high flux neutron and X-ray sources and technological improvement in thin film multilayer devices required for focussing and monochromatisation of these sources. Monochromatic, polarized, collimated and focused beam at different sample environments have been achieved by such thin film multilayer devices^{1,2}. Multilayer thin film devices operate on the principle of Bragg reflection. The multilayers can be periodic as shown in Fig 1(a) or non-periodic as shown in Fig 1(b). By creating periodic artificial contrast in neutron scattering length high reflection can be achieved by Bragg principle. In non-periodic multilayers hundreds of layers are arranged in such a fashion that all these Bragg peaks merge and a high reflectivity is achieved continuously over a large angular range. This device is also known as super mirror and it is normally designated by its *m*-value which is defined as the ratio of critical angle of the super mirror compared to that of natural Ni¹. In some special material combination of the super mirror it

can be used for spin polarization of neutron as well as for analysing spin of scattered neutron. Similarly, multilayer with electron density contrast can generate high X-ray

reflection. Such multilayers have applications as optical element in lithography, spectroscopy, microscopy and free electron laser experiments². Recently it has shown promise as soft γ -ray mirror also in the non-destructive assay (NDA) of spent nuclear fuel.

Multilayer development facilities

Fabrication of such multilayer structures with layer thickness of the order of nm and sub-nm is a big technological challenge particularly to maintain thickness uniformity over hundreds of layers and to maintain the desired surface and interface morphology. In multilayer devices the surface roughness and

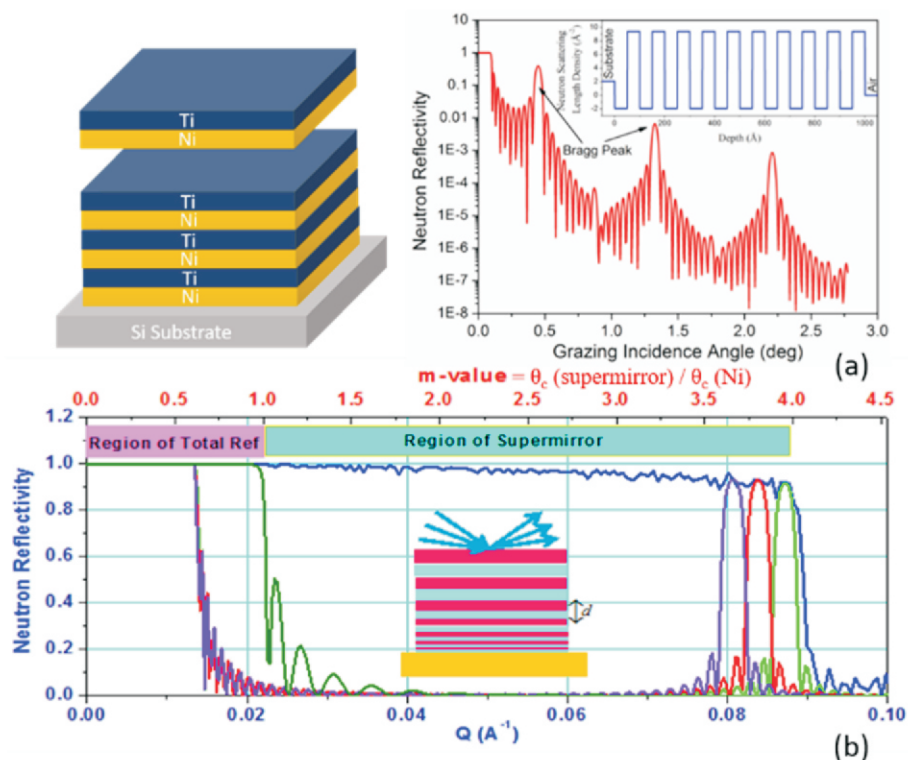


Fig. 1: Structure and neutron reflectivity of (a) periodic multilayer (b) non-periodic multilayer or supermirror

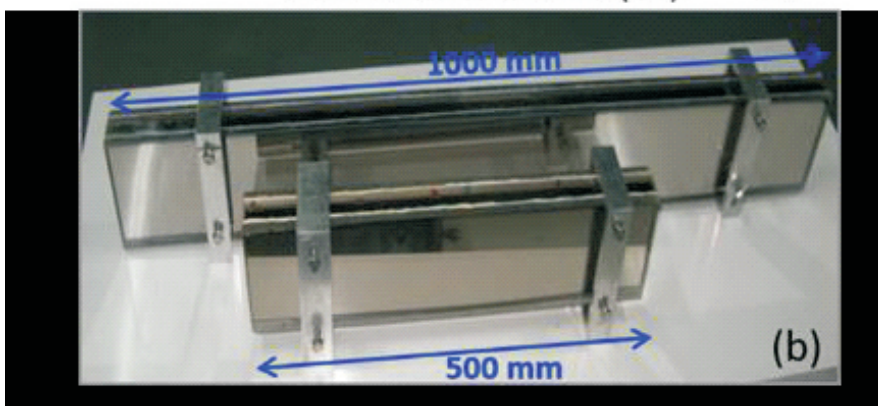
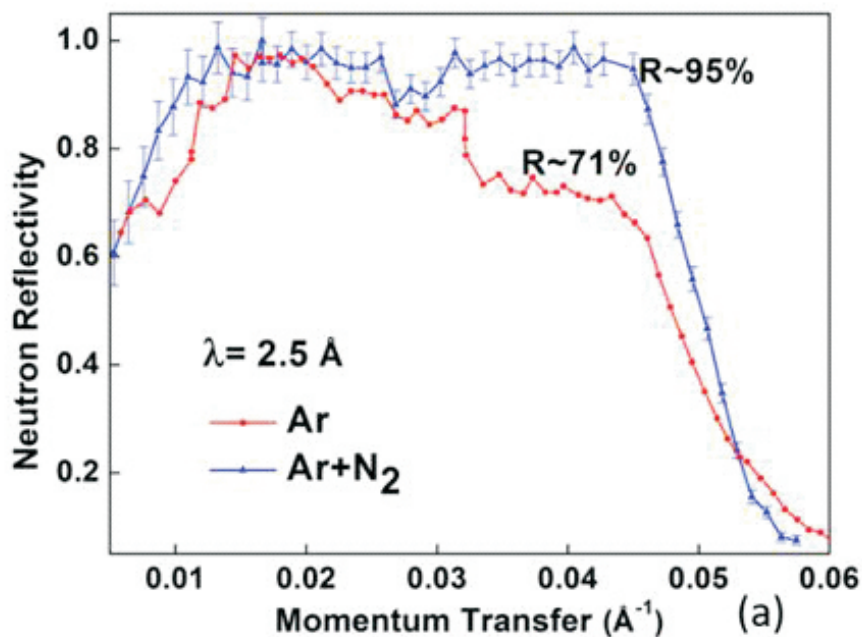


Fig. 2: (a) Measured neutron reflectivity of 98-layer $m=2.0$ neutron supermirror deposited under pure Ar and $Ar+N_2$ ambience (b) Prototype 500 mm long supermirror guide tube element for DHRUVA

interface roughness should be maintained below 1 nm throughout the structure to prevent scattering losses. In application of low grazing incidence angle X-ray mirror large size mirrors are essential to cover the whole foot print of the X-ray beam from a synchrotron source. In our laboratory, magnetron sputtering and ion beam sputtering techniques are being used for the development of such multilayers since sputtering techniques yield higher adatom energies at the substrate surface which ultimately results in smoother surface and interfaces in the multilayers. A 9 m long DC/RF magnetron sputtering large area coating system (LACS) has been designed and built indigenously in our laboratory for this purpose³. The fully automated computer-controlled system is capable of depositing more than 500-layer multilayer thin films on substrate of maximum dimension 200 mm x 1500 mm following a pre-determined recipe without manual intervention. A state-of-art Dual Ion Beam

sputtering (DIBS) system IonSys-800 (Meyer Burger, Germany) has also been installed in our laboratory recently which can deposit layers with sub nm precision and bulk-like density. Using these two systems recently we have developed several neutron supermirrors, neutron supermirror polarizers, Synchrotron X-ray mirrors, soft X-ray mirrors for XUV and water window region which have various applications in condensed matter research. Few examples are given below:

Neutron Supermirror

Neutron supermirrors can be used for fabricating neutron guide tubes which can deliver neutrons from source to the experimental station with higher flux. Also curved supermirrors can be used for focusing neutrons on samples with a spot size $\sim 100 \mu m^4$. Using the in-house developed 9 m long magnetron sputtering system of our laboratory, 98-layer $m=2.0$

Ni/Ti neutron supermirrors have been developed following the design carried out by an in-house developed code⁵. The reflectivity of the supermirrors have been improved significantly to 95% by depositing the Ni layers of the multilayers under a mixed ambience of $Ar+N_2$ instead of under pure Ar ambience. The neutron reflectivity of two supermirrors deposited with under pure Ar and under $Ar+N_2$ mixed ambience are shown in Fig 2(a), Fig.2(b) shows the photographs of 1000 mm and 500 mm long Ni/Ti supermirrors produced for applications in guide tubes of DHRUVA.

In order to investigate the reason for increase of neutron reflectivity of Ni/Ti supermirror due to deposition of Ni layer in ambience of $Ar+N_2$ several periodic multilayers are deposited at similar condition and characterized by grazing incidence X-ray reflectivity (GIXRR), X-Ray Diffraction (XRD), grazing incidence extended X-ray absorption fine structure (GI-EXAFS) and grazing incidence X-ray fluorescence (GIXRF) techniques^{6,7}. In Fig 3(a), GIXRR of 10-bilayer Ni/Ti periodic multilayers deposited under pure Ar ambience and under mixed ambience of $Ar+N_2$ are shown. By fitting these data it is found the Ni-on-Ti interface width decrease from 0.5 nm to 0.4 nm and Ti-on-Ni interface width decreases from 0.7 nm to 0.2 nm upon deposition under mixed ambience. X-ray diffused scattering measurements on the multilayers show that the reduction of this roughness is more due to reduction of interface diffusion. These two multilayers also characterized by GIEXAFS technique at Ni K-edge using BL-9 beamline Indus-2 as shown in Fig 3(b). This again manifests less interface diffusion in multilayer deposited under mixed ambience with $Ar+N_2$. XRD patterns of the two multilayers, as shown in Fig 3(c), reveal that the reduction in diffusion is due to formation of amorphous Ni layer when sputtered under mixed ambience of $Ar+N_2$. Nuclear resonance reaction (NRR) studies reveal that presence of nitrogen in Ni lattice leads to amorphisation of Ni layers which ultimately leads to less interface diffusion. Element specific diffusion of the Ni and Ti have been investigated using GIXRF technique at as shown in Fig 3(d), analysis of which also shows that at interfaces the change in Ni concentration is sharper in the multilayer deposited under $Ar+N_2$ mixed ambience compared to the multilayer deposited under pure Ar ambience.

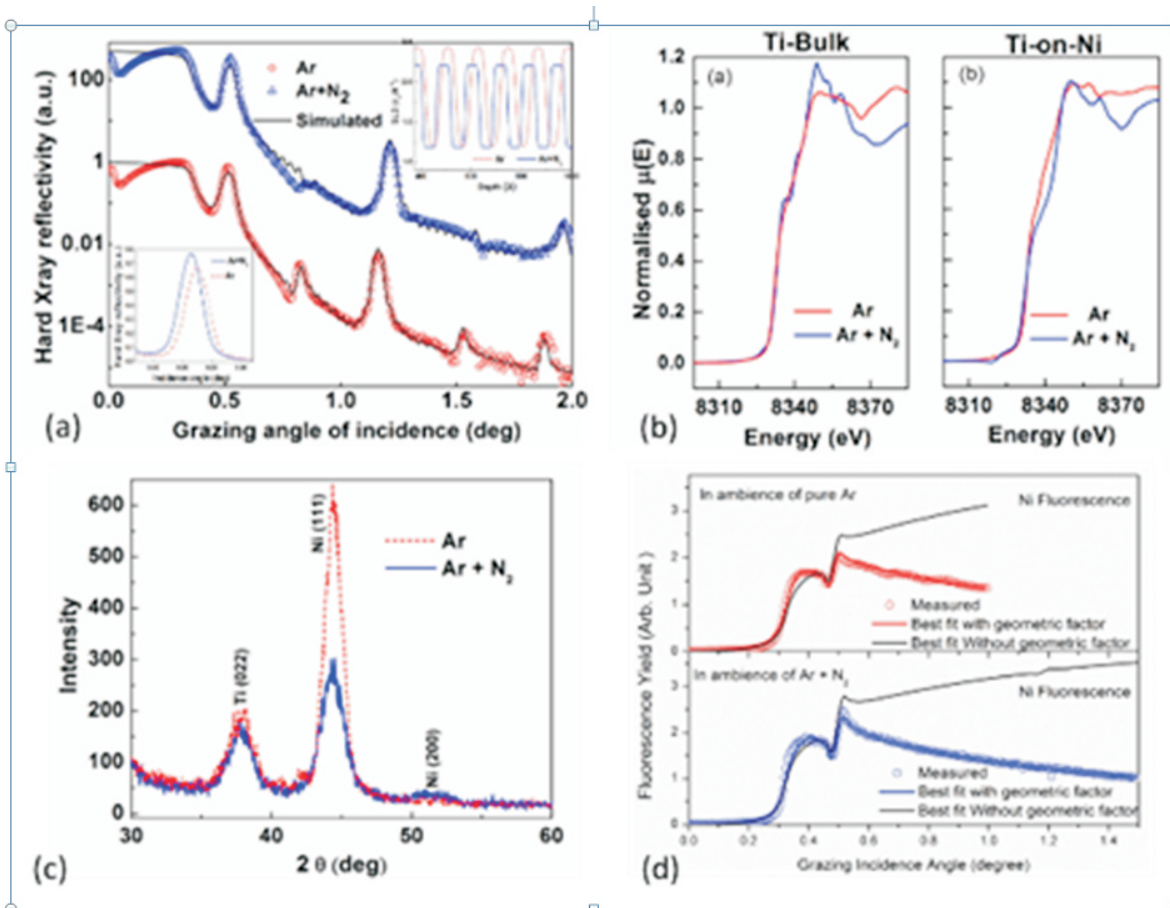
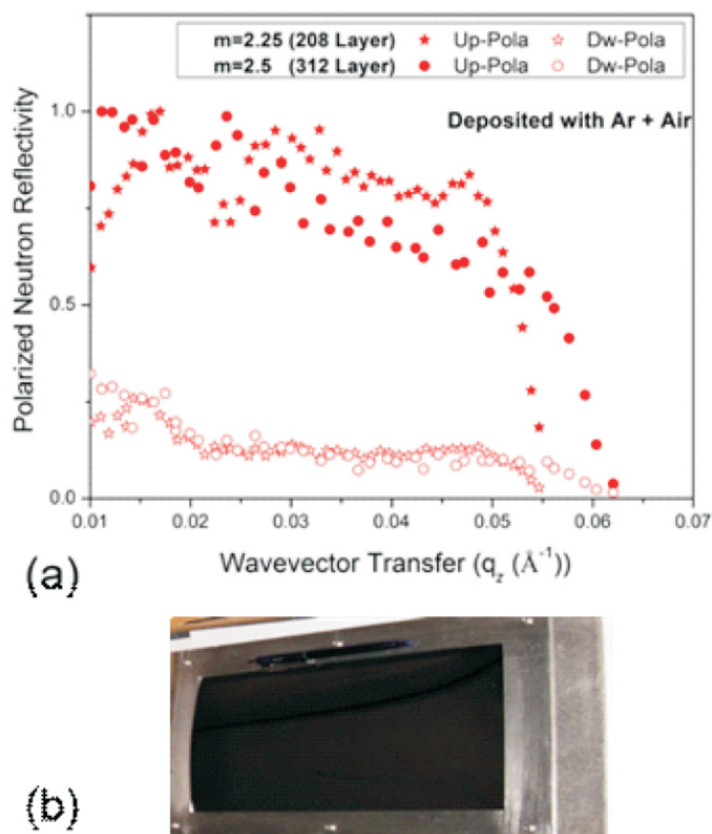


Fig. 3: Characterization of Ni/Ti periodic multilayer deposited under Ar and under mixed ambience of Ar+N₂ (a) GIXRR (b) GIEXAFS (c) XRD (d) GIXRF



Neutron Supermirror polarizer

In a supermirror polarizer alternate layers of magnetic and non-magnetic materials are chosen such that neutrons with spin polarization in the direction of the magnetization get reflected from the multilayer and neutrons with spin polarization in the opposite directions pass through it. These devices are used to polarize the neutron beam in neutron scattering experiment as well as to analyse the spin of scattered neutrons from a sample, like in a spin echo measurement. Using the 9 m long magnetron sputtering system Co/Ti supermirror polarizers of $m=2.25$ (208 layer) and $m=2.5$ (312 layer) have been developed⁹. It is found that the polarized reflectivity of the supermirror improves when Co layers are deposited in under mixed ambience of Ar and air. In Fig 4(a) the polarized neutron reflectivity (PNR) spectra of these supermirrors are shown. At this condition Co/Ti supermirror polarizers are developed on both sides of 500 μm thick glass substrates having dimension of 141 mm x 251 mm, a photograph of which is shown in Fig 4(b). The cross sectional TEM micrographs of two $m=2.5$ supermirrors

Fig. 4: (a) $m=2.25$ and $m=2.5$ Co/Ti supermirror polarizer (b) A Co/Ti supermirror polarizer having dimension of 251 mm x 141 mm element.

Crosse sectional TEM of m=2.5 Co/Ti Supermirror

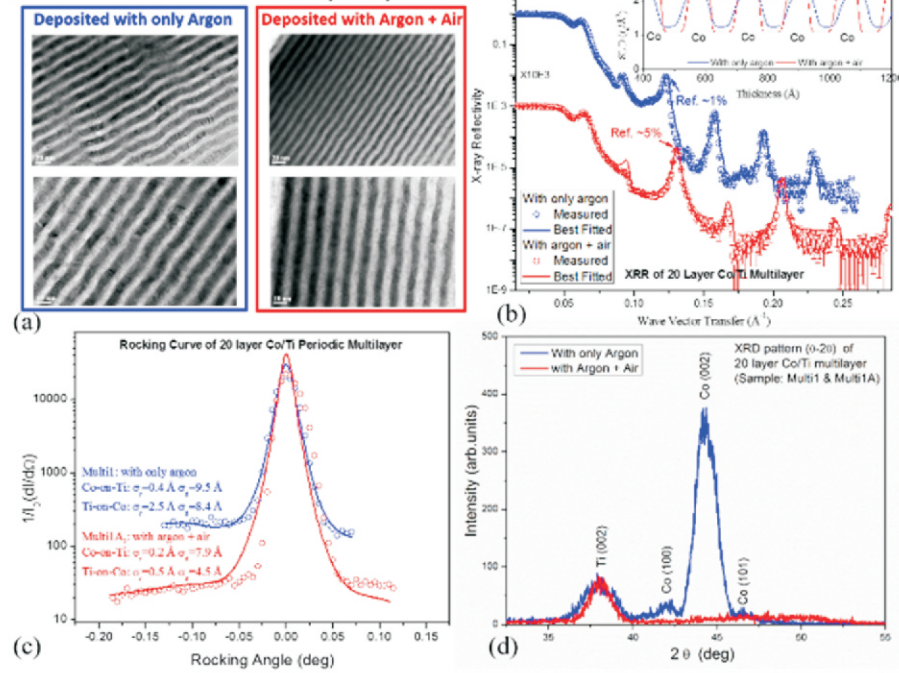


Fig. 5: Characterization of Co/Ti multilayer prepared under pure Ar ambience and under mixed ambience of Ar+air (a) TEM of m=2.5 supermirrors (b) XRR of periodic multilayers (c) rocking scan of periodic multilayers and (d) XRD of periodic multilayers.

are shown in Fig 5(a), it is seen that the layers are wavier in the supermirror deposited under pure Ar ambience compared to the supermirror deposited under mixed ambience of Ar and air, which also has relatively sharper interfaces. Further investigations have been done by preparing 20 layer Co/Ti periodic multilayers and characterizing them by GIXRR, PNR and XRD techniques⁹. In Fig 5(b) it is seen that the Co-on-Ti and Ti-on-Co interface widths decrease when Co layers are sputtered under mixed ambience of Ar and air, also the SLD at the interfaces are found to be sharper with higher contrast. Diffused X-ray scattering measurements at grazing incidence are shown in Fig 5(c), analysis of which reveal that this change of interface width is due to reduction of interface diffusion. XRD patterns of these two multilayers shown in Fig 5(d) reveal that the reduction of interface diffusion or waviness is due to amorphization of Co layer when sputtered under mixed ambience of Ar and air.

Synchrotron X-ray Mirror

In Synchrotron beamlines grazing incidence mirror are very much essential for collimation and focusing of the beam since reflectivity of X-rays is very high at grazing angle of incidence. As these mirrors work at very low grazing angle on

the principle of total external reflection, the lengths of these mirrors are generally large (1000mm or above) to cover the footprint of the whole SR beam. Using the in-house developed 9m long LACS system Cr/Au synchrotron mirrors have been deposited on plane (500 mm x 51 mm x 51 mm) and spheroidal (300 mm x 51 mm x 47 mm) zerodour substrates⁹. In Fig. 6 the hard X-ray (0.154 nm) reflectivity, soft X-ray reflectivity and the photograph of the

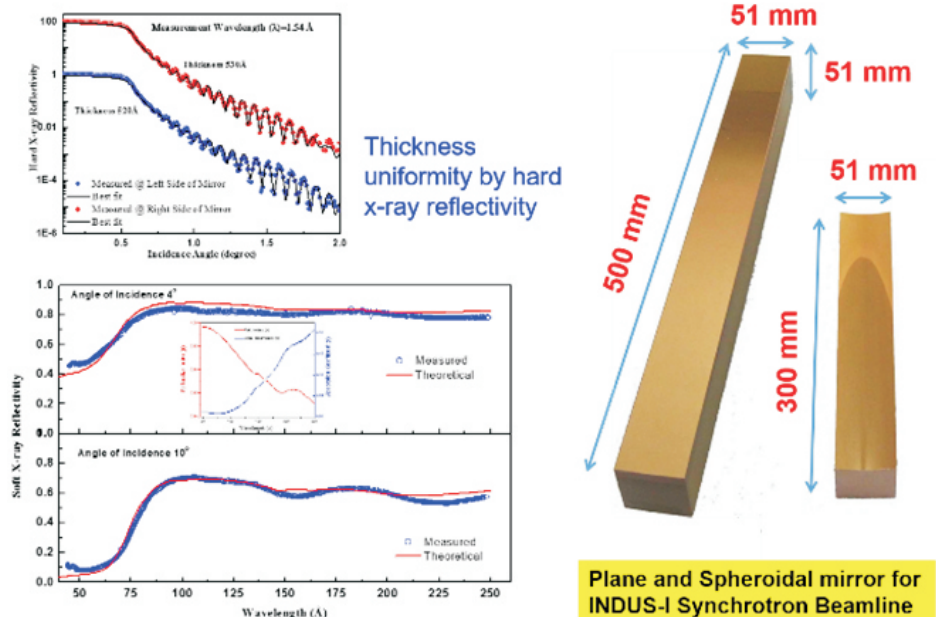


Fig. 6: Hard X-ray and soft X-ray reflectivities of Cr/Au grazing incidence Synchrotron mirror for PAS beam line at Indus-1SRS.

mirrors are shown. The soft X-ray reflectivities of the mirrors are found to agree well with theoretical simulations. These mirrors have been installed at the PAS beamline of Indus-1 SRS.

EUV and SXR Multilayer Mirror

X-ray multilayer mirrors are also essential for reflecting and monochromatising extreme ultra violet (EUV) and soft X-ray (SXR) (1-60 nm) wavelengths since in this region natural crystals and gratings are not available². Apart from applications as optical components in beamlines of synchrotron and free electron laser sources, these mirrors have some other specific practical applications. For example, in EUV lithography systems where soft X-ray radiation from 6-14 nm are used and in soft X-ray microscopes operating in the water window region of 2.3–4.4 nm, where water is transmissive but carbon based organic materials shows strong absorption, these multilayer mirrors have acquired great interest. Using the DIBS system of our laboratory, Mo/Si multilayers with bi-layer thickness of 7 nm have been developed which can reflect 13 nm wavelength at higher grazing angle of incidence. In Fig. 7(a) and (b) the hard X-ray and soft X-ray reflectivities of the 25 bi-layer Mo/Si multilayers are respectively shown. It is found that the multilayer deposited with C buffer layer at the Mo/Si interfaces has better reflectivity than that deposited without the buffer layer. The Mo/Si multilayer with C buffer layer has achieved

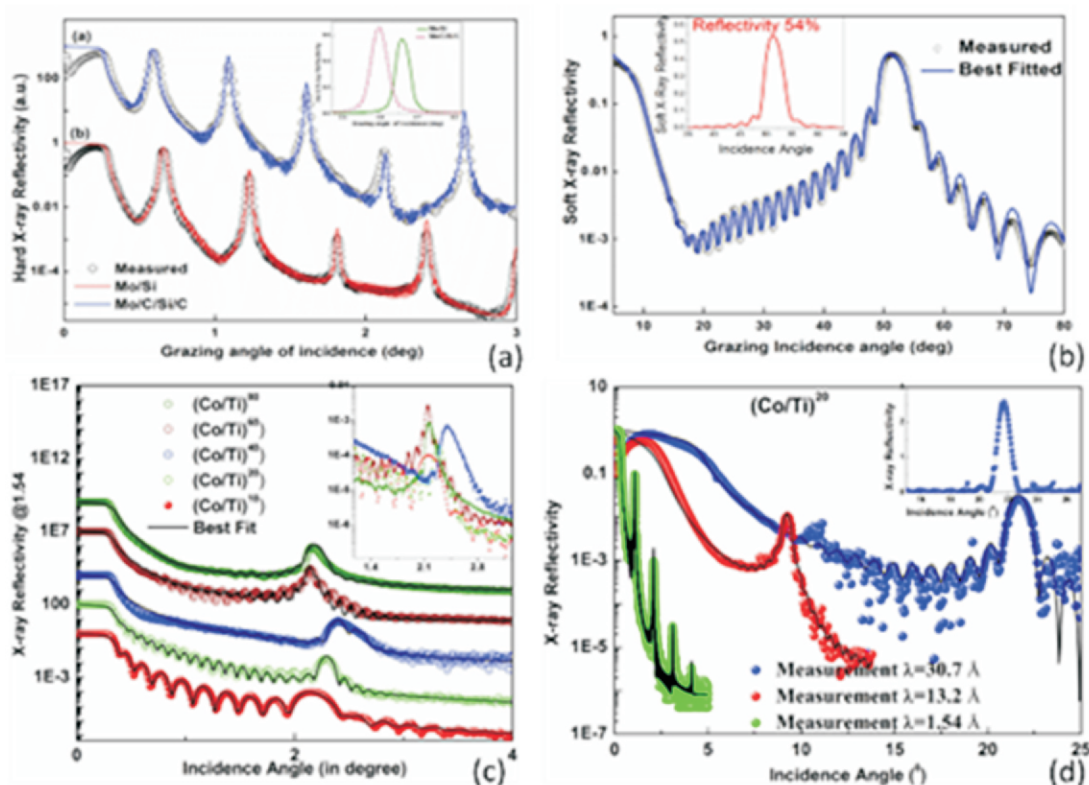


Fig. 7: (a) Hard X-ray (b) Soft X-ray reflectivities of 25 bi-layer pair Mo/Si multilayer for EUV lithography application. (c) Hard X-ray (d) Soft X-ray reflectivities of Co/Ti multilayers for water window application.

54% reflectivity at 51° grazing angle of incidence¹⁰. Further GIXAFS measurements with Indus-2 SRS confirm lowering of interface diffusion in this multilayer due to the presence of C buffer layer.

For applications in water window region however, due to lower value of the probing wavelength (2.2-4.4 nm) multilayers with lower bilayer thickness are required. Co/Ti multilayers with low bi-layer thickness of 1.8 nm (with nominally 0.9 nm of Co and 0.9 nm of Ti layers) have been deposited in the LACS system with a specially designed SS mask, placed below the target at a distance of 50 mm which reduces the exposed length of the target along the direction of the substrate trolley movement. The variation of hard X-ray reflectivity of Co/Ti multilayer samples with no. of layers are shown in Fig.7(c) which shows that maximum reflectivity is obtained for the 60 bi-layer sample¹¹. Fig.7(d) shows that reflectivity of 2.5% has been obtained for the Co/Ti multilayer sample at 21.5° grazing angle of incidence and for 3.07nm of soft X-ray wavelength¹².

Using the DIBS system Cr/Ti multilayers with bi-layer thickness ranging from 3.8 nm to 2.1 nm with an optimised Cr to bi-layer thickness ratio of 0.4 have been

deposited. Fig. 8(a) and (b) show the variation in the diffused X-ray scattering spectra and Cross-sectional TEM micrographs of Cr/Ti multilayers with different bi-layer thicknesses. From the above measurements it could be concluded that for all the ML samples Ti

layer thickness is higher than 1.3 nm and Ti forms continuous layer on Cr for all cases. However, Cr layer thickness varies from 1.5-0.8 nm in the above range of bi-layer thickness and Cr undergoes continuous-to-discontinuous transition as the layer thickness reduces below 1 nm¹³.

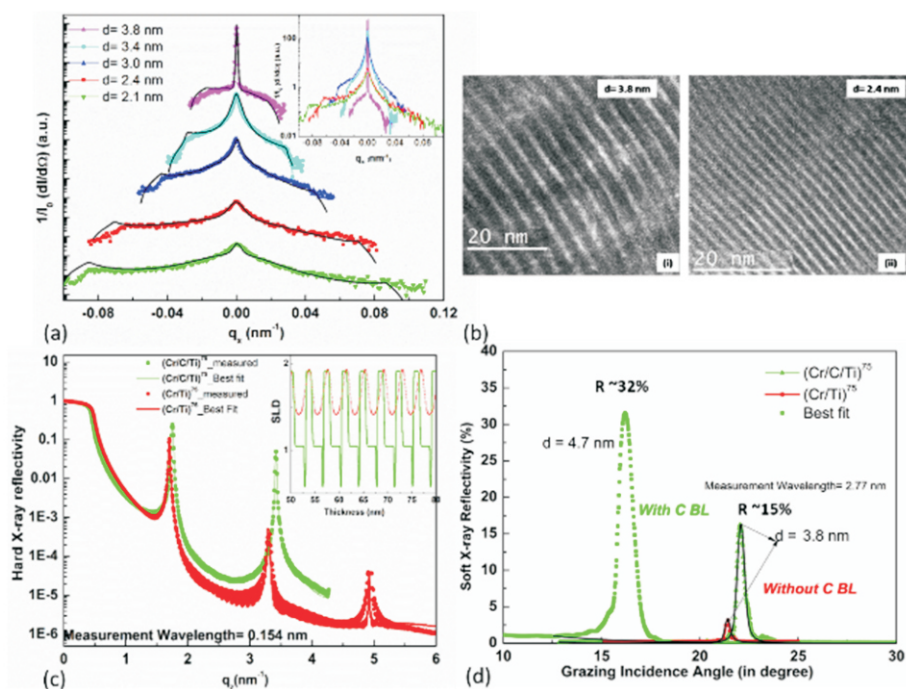


Fig. 8: Characterization of Cr/Ti multilayer (a) Diffused X-ray scattering (b) Cross sectional TEM (c) Hard X-ray reflectivity (d) Soft X-ray reflectivity

The hard X-ray and soft X-ray reflectivities of Cr/Ti periodic multilayers with and without C buffer layers at the interfaces are shown in Fig. 8(c) and 8(d). It can also be seen from the above figure that for a Cr/C/Ti multilayer of slightly higher bilayer thickness of 4.7 nm, very high (~31.6%) reflectivity for 16.2° grazing angle of incidence can be obtained at water window soft X-ray wavelength of 2.77 nm, which is the highest reflectivity reported so far in the literature in this wavelength regime¹⁴.

Summary

Development of multilayer optics is indispensable in the condensed matter research using neutrons and X-rays as probe. Over the years a comprehensive facility has been created at A&MPD, BARC consisting of the in-house developed large area coating system (LACS) and the commercially procured DIBS system, for fabrication of these multilayer devices with sub-nm level control over thickness and interface morphology. Using the above facility non-periodic Ni/Ti neutron supermirrors and Co/Ti supermirror polarizers have been developed for application in neutron optics, while 1.5m long Cr/Au grazing incidence Synchrotron X-ray mirror, Mo/Si multilayer mirrors for soft X-ray EUV applications and Co/Ti and Cr/Ti multilayer mirrors for soft X-ray water-window applications have been successfully developed. In each of the above cases by optimizing the process condition or introducing buffer layer at the interfaces the performance of the multilayer device has been improved to the quality comparable to or better than that reported so far in the literature.

Corresponding Author*
Dibyendu Bhattacharyya
(dibyendu@barc.gov.in)

References

- [1] Masahiko Utsuro, Vladimir K. Ignatovich, Handbook of Neutron Optics, Wiley-VCH; 1st edition (2010).
- [2] Sáenz-Trevizo A and Hodge A M, Nanotechnology 31 (2020) **292002**.
- [3] A. Biswas, R. Sampath kumar A. Kumar, D. Bhattacharyya, N.K. Sahoo, K.D. Lagoo, R.D. Veerapur, M. Padmanabhan M., R.K. Puri, D. Bhattacharya, S. Singh and S. Basu, Rev. Sci. Instrum. 85 (2014) **123103**.
- [4] Takuya Hosobata, Norifumi L. Yamada, Masahiro Hino, Yutaka Yamagata, Toshihide Kawai, Hisao Yoshinaga, Koichiro Hori, Masahiro Takeda, Shin Takeda and Shin-ya Morita, Opt. Express 25 (2017) **20012-20024**.
- [5] Abharana N, A. Biswas, P. Sarkar, S. Rai, S. Singh, S. Kumar, S.N. Jha and D. Bhattacharyya, Vacuum 169 (2019) **108864**.
- [6] A. Biswas, Abharana N, S. Rai and D. Bhattacharyya, J. Appl. Phys. 127 (2020) **165304**.
- [7] A. Biswas, Abharana N, S.N. Jha and D. Bhattacharyya, Appl. Surf. Sci. 542 (2021) **148733**.
- [8] A. Biswas A.K. Porwal, D. Bhattacharya, C.L. Prajapat, A. Ghosh A, ManglaNand, C. Nayak, S. Rai, S.N. Jha, M.R. Singh, D. Bhattacharyya. S. Basu and N.K. Sahoo, Appl. Surf. Sci. 416 (2017) **168–177**.
- [9] P. Sarkar Roy, A. Biswas, Debarati Bhattacharya, R. K. Sharma, M. H. Modi, S. Rai, D. Bhattacharyya and N. K. Sahoo, AIP Conference Proceedings 1832, **060011** (2017)
- [10] N Abharana, A. Biswas, P. Sarkar, P. Rajput, Rajnarayan De, K.D. Rao, M.H. Modi, D. Bhattacharyya, S.N. Jha and N.K. Sahoo, Thin Solid Films 673 (2019) **126-135**
- [11] P. Sarkar, A. Biswas, S. Ghosh, S. Rai, M.H. Modi and D. Bhattacharyya, Thin Solid Films 693 (2020) **137688**.
- [12] P. Sarkar, A. Biswas, Rajnarayan De, K.D. Rao, S. Ghosh, M.H. Modi, Siju, H.C. Barshila, D. Bhattacharyya and N.K. Sahoo Appl. Optics 56 (2017) **7525-7532**.
- [13] P. Sarkar, A. Biswas, S. Rai S, H. Srivastava, S. Mandal, M.H. Modi and D. Bhattacharyya, Vacuum 181 (2020) **109610**.
- [14] P. Sarkar, A. Biswas, Abharana N, S. Rai, M.H. Modi and D. Bhattacharyya, J. Synchr. Rad. 28 (2021) **224-230**.

Integrated Hydrogen gas sensing device Based on sputter-deposited Pd thin films

*Niyanta Datta¹, S. Samanta¹, S. Bhattacharya¹, Ankita Pathak¹,
N. Ramgir¹, Kailasa Ganpathi¹, Manmeet Kaur¹, K.P. Muthe¹, A.K. Debnath¹,
Deepa Bhambure², P. Abichandani²

¹Technical Physics Division

²Electromagnetic Application & Instrumentation Division

Bhabha Atomic Research Centre, Mumbai – 400 085

Abstract

Pd thin film based hydrogen (H₂) gas sensor device working on Pellister-type principle has been developed. The sensor consists of Pt-100 heater coated with RF sputtered Pd thin film (100 nm). The device operates at 150°C in sensor-compensator configuration in a Wheatstone bridge that makes it sensitive to small temperature increments caused due to the presence of H₂ gas. The response of the sensor is integrated with a digital monitor displaying the calibrated values of H₂ gas concentration (independently confirmed using ultrasonic transducer). The sensor device exhibits a minimum detection limit of 0.3% with linear response (0-3.5% H₂), tested in an in-house made dynamic gas sensing set up. The indigenously developed sensor device exhibits reliability, precision, long term stability and consequently a long lifespan > 3 years and is currently being utilized by various users within and outside DAE.

Keywords: RF sputtered Pd thin film, Catalytic, H₂ sensor, Lower explosive limit

Introduction

Environmental sustainability of the energy sources has been the defining foundation of many recent scientific and technology development activities. Consequently, several research groups are rigorously trying to find out alternate solutions to this crisis-like-situation through techniques, which are by and large green and do not add to the existing carbon footprint. In this context, it is probably worth mentioning that Hydrogen (H₂) based energy generation has been a globally accepted practice for obtaining clean energy. Being a clean source of energy, H₂ gas is in high demand in various industrial and commercial applications. However, H₂ is an explosive gas and it is colorless and odorless. The flammability of H₂ is in the range of 4 – 75 % in air. In presence of an oxidizer, hydrogen catches fire explosively. Its 4% (v/v) mixture in air forms lower explosive limit (LEL) and 75% (v/v) is the upper explosive limit (UEL). H₂ gas is used for various sorts of industrial applications such as hydro-desulfurization

and hydrocracking operation in refineries, ammonia production, metallic ore reduction, rotor coolant in large electrical generator etc. Further, the small sized gas molecules of H₂ are prone to leak through

the smallest possible holes and cracks. Hence, the detection of H₂ gas becomes essential even at trace levels in nuclear reactors, power plants, battery house, terminal ballistic research laboratories etc. The production, uses, storage and transportation of hydrogen gas are very risky without sensor. Hence, the H₂ gas monitoring is highly essential in various applications to ensure safety of national property and human life.

There are many methods for detection of H₂ gas as schematically shown in Figure 1. Most of the methods show good response; however they suffer from shortcomings like large size and weight, high cost, time consuming process, requirement of trained personnel to operate them, maintenance and portability

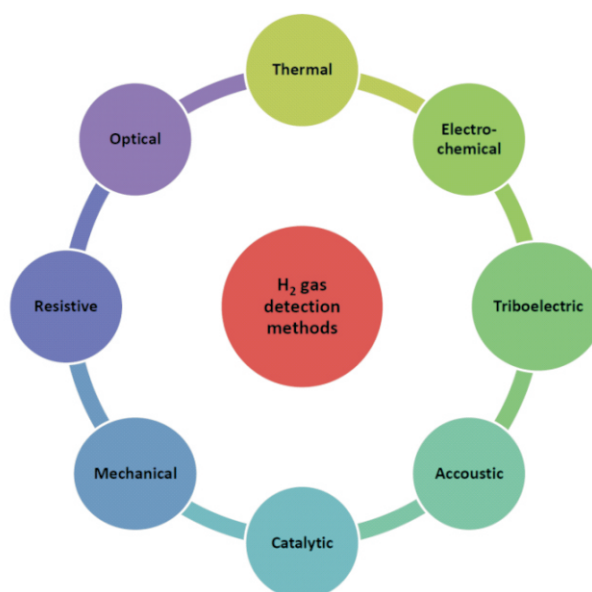


Fig. 1: Schematic diagram representing the methods for H₂ detection.

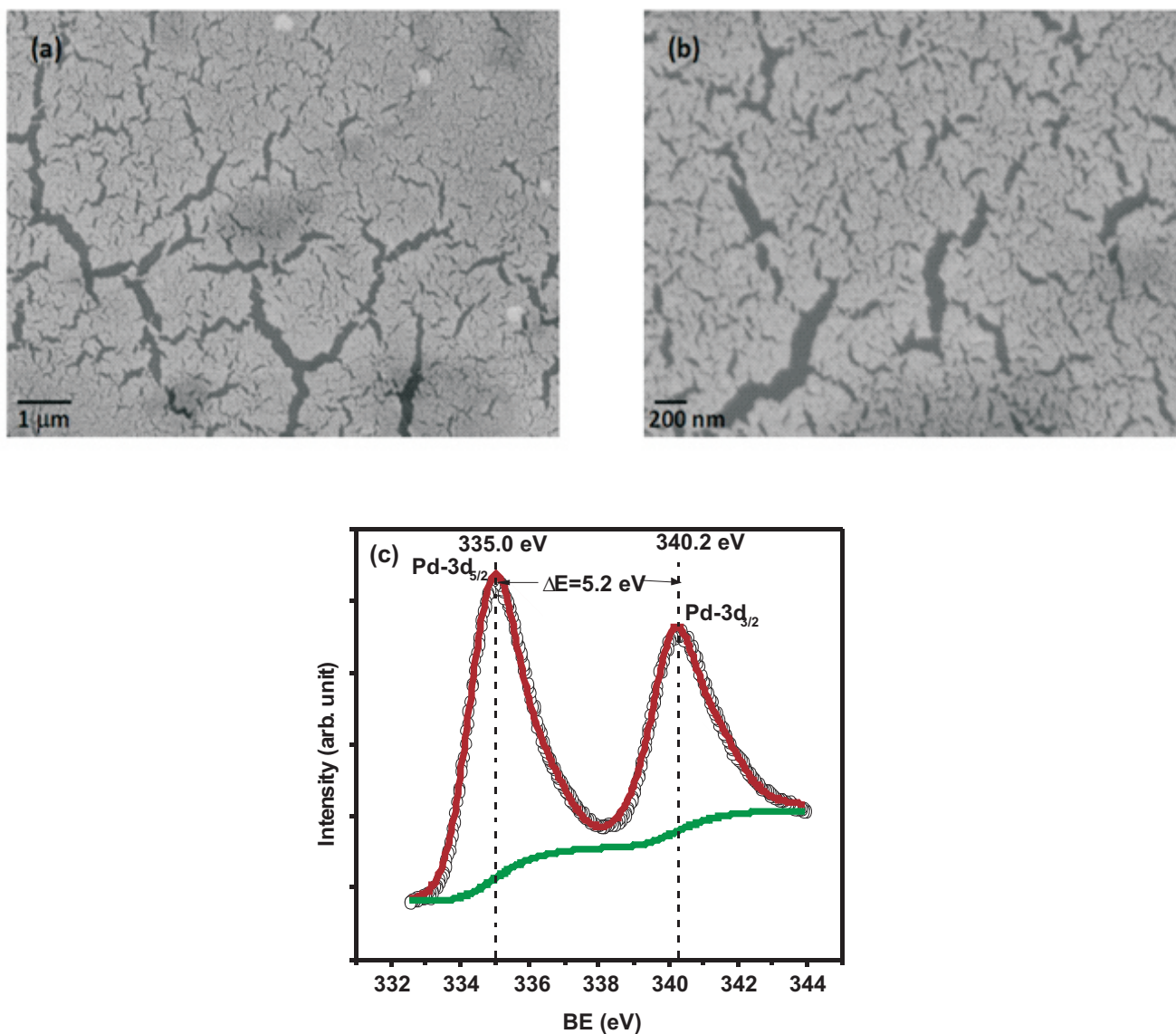


Fig.2: SEM image of as-deposited Pd films on Pt-100 heater at (a) m scale, (b) nano scale (c) XPS spectrum of Pd-3d peak.

issues etc. The above mentioned limitations restrict the continuous operation of such instruments. Both resistive and optical sensors are based on the principle of formation of PdH, leading to surface deformation of the sensor film that may pose repeatability and reliability issues. Although electrochemical type sensors are very sensitive but this type of sensors have short lifespan and narrow range of operating temperature i.e. calibration is highly susceptible to the variation of ambient temperature. Also, triboelectric and mechanical methods of detection are more suitable for lower concentrations. On the contrary, catalytic type sensor operated at an elevated temperature has many advantages such as long lifespan, robustness, simple to operate, easy to install, calibrate and operational in the range of 0-4% H₂ concentration. Catalytic type sensor by

Figaro is commercially available with detection range of 30-1000 ppm exhibiting a power consumption of 660mW. Pellistor type Pt/Pd based catalytic sensors are well known to be suitable for hydrogen detection. In this report, we discuss the device development of Pd thin films based H₂ sensor at Technical Physics Division, in collaboration with Electromagnetic Application & Instrumentation Division.

Deposition of Pd films

Standard Pt-100 heaters (10 mm x 2 mm) were used as substrates to fabricate sensor elements. Pd layer of 100 nm (confirmed using a profilometer for thickness measurement) thickness was deposited on both sides of Pt-100 using rf sputtering (photograph shown in Fig. 4(c)). The deposition was carried out at 20W for 8 min under Ar pressure of 0.08

mbar. Fig. 2(a) and (b) shows the scanning electron microscopy (SEM) images of as-deposited Pd-films on Pt-100 heater surface. As clearly seen, the film is very smooth with visible nano cracks which may be attributed to interfacial stress due to lattice mismatch and which may be responsible for better gas diffusion and excellent sensor response towards H₂ gas owing to enhanced surface area to volume ratio. The metallic nature of Pd film was confirmed by X-ray photoelectron spectroscopy (XPS). The Pd-3d_{5/2} peak (Fig. 2(c)) position at 335.0 eV and E ~ 5.2 eV confirm the zero valence state of Pd i.e. metallic nature.

Working Principle and Device Configuration

The sensor element (Pd coated Pt-100) and a compensator element (Pt-100)

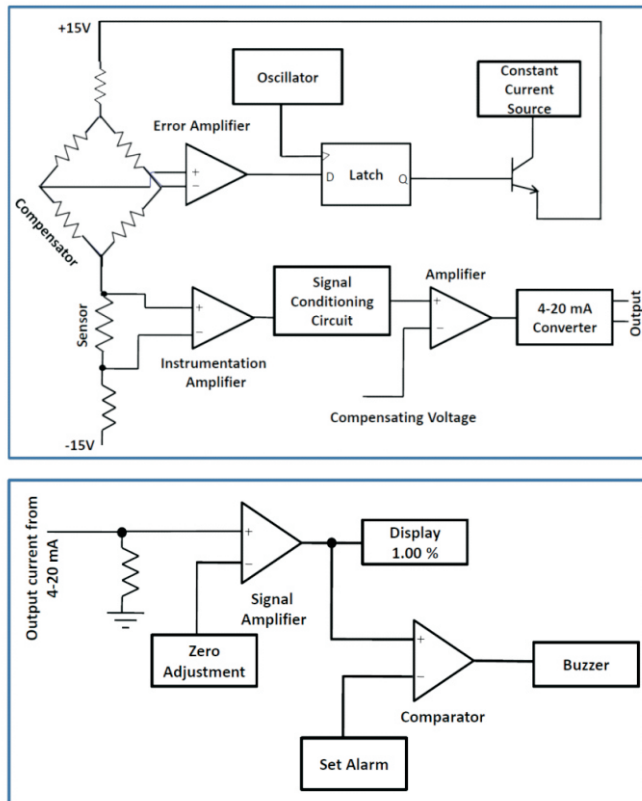


Fig. 3: Block diagram of in-house designed sensor device, (a) sensor unit, and (b) Monitor unit.

are connected in the Wheatstone bridge of an in-house designed temperature controller circuit, whose block diagram is shown in Fig.3(a). The oscillator to yield forced oscillation time that curbs constant current mode. The exothermic reaction of H_2 with O_2 , $2H_2 + O_2 \rightarrow 2H_2O + 285 \text{ kJ/mol}$, on the sensing element (containing Pd as catalyst, facilitating low heat of adsorption of oxygen on their surface) causes rise in

temperature w.r.t the compensator. The circuit transforms the change in temperature of the sensor element into voltage developed between sensor and compensator that is calibrated against H_2 concentration and displayed through an integrated monitor, depicted in Fig. 3(b).

The output voltage is then converted into 4-20 mA using a monolithic current

transmitter (AD694 IC). The 4-20 mA current loop helps to keep the sensor away from the control room (< 300 m) where H_2 concentration can be monitored remotely. This facilitates customization of the sensor device unit as per the requirement of different monitoring conditions of users.

The 4-20 mA current is converted into 0-5V with a single terminating resistance, and this voltage is attenuated and displayed as a sensor response directly related to vol. % of H_2 concentration in an integrated monitor unit. With the help of zero potentiometer on the front panel, the zero on the display is adjusted in the absence of hydrogen. The integrated monitor unit also has the provision for alarm setting that can be set as per the user requirement. The actual photographs of the sensor device are shown in Fig. 4. The sensor device consists of a sensor unit (Fig. 4(a) & (b)) in which sensing element (Fig. 4(c)) and compensator along with temperature controller circuit are concealed. This unit is mounted at the location of H_2 gas leakage. The other part is an integrated digital monitor (Fig. 4(a) below the sensor unit) displaying output voltage (calibrated as actual H_2 gas conc.) to be placed at the location of monitoring with provisions of alarm and zero set.

Sensor Calibration

The hydrogen sensing was studied in a dynamical gas sensing set up shown in Fig.5. The H_2 gas was used from a hydrogen generator (Model CIC-PW-SPE500HC) based on the principle of electrolytic splitting of water, and air was used from an oil free air compressor. The H_2 and air were mixed in the desired ratio, to generate various H_2 concentrations (0-3.5 %), and made to flow through the sensor housing mounted in the setup and directed to the exhaust after sensor exposure. To ensure safety measures we did not cross 3.5 % H_2 during calibration in the laboratory. The mass flow controllers (MFC's) and rotameters were used to set the H_2 flow in the 0-30 cm^3 range and air flow in 0-400 cm^3 range. The sensors were calibrated against an ultrasonic transducer which can measure time of flight with resolution of 10 ns. It is a pulse receiver model 4400 MX from Roop Telesonic Ultrasonix Ltd. Mumbai.

It works on the principle of time of flight measurement. The transducer is excited at a frequency of 500 kHz in pulse

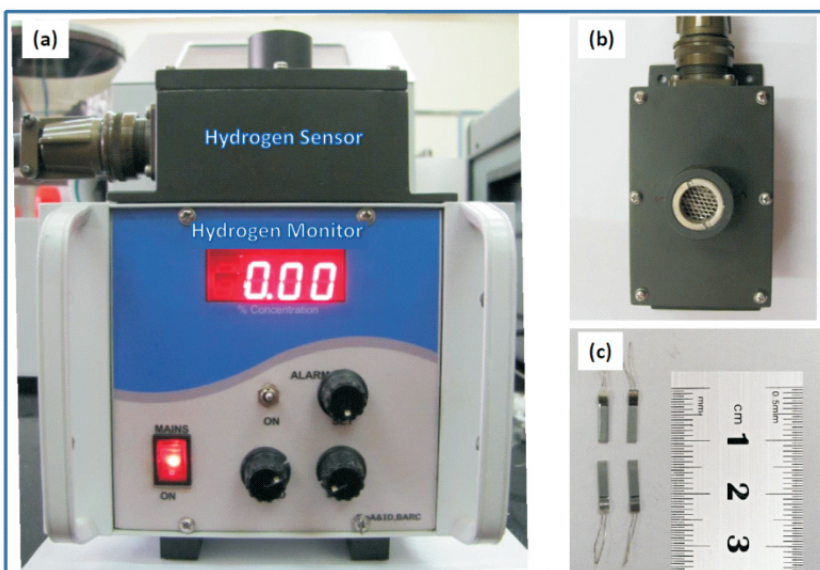


Fig. 4: (a) The complete sensor device with sensor mount on top of monitor displaying output voltage (corresponding to H_2 % conc.), (b) top-view of the sensor mount to be installed at the location of H_2 leakage and (c) Pd films deposited on Pt-100 heaters.

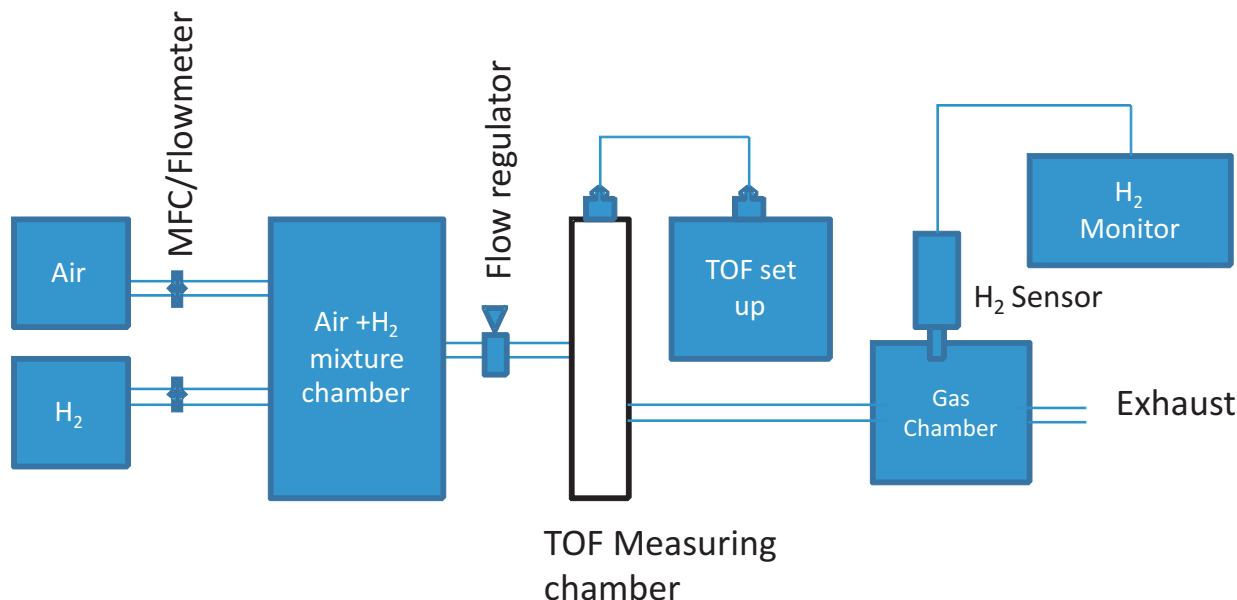


Fig. 5: : Schematic of dynamic H₂ gas sensing set-up.

mode and it detects the echo of the reflected signal at the piezoelectric crystal. The velocity of ultrasonic sound in gas mixtures is dependent on the concentration or the volume percentage of hydrogen (H₂) in the mixture, which is governed by the formula of classical sound velocity as indicated in the following equation:

$$v = \sqrt{\frac{\gamma RT}{M}}$$

where γ (~1.41 for H₂ and air), R, T, and M are the heat capacity ratio (C_p/C_v), gas constant, temperature, and the molecular weight of gas, respectively. In practical experiment, air is commonly used as background gas, and Eq. (1) can be rewritten as:

$$v = \sqrt{\frac{\gamma RT}{M_{air} \cdot (1 - \rho) + M_{H_2} \cdot \rho}}$$

where the molecular weight of nitrogen M_{air} is 28.97, the molecular weight of hydrogen M_{Hydrogen gas} is 2.02, and the volume ratio of H₂ is (0%, 1%, etc.). The velocity of sound in air ~ 350 m/sec and in H₂ ~ 1270 m/sec. The calculated value for air (H₂ = 0%) is 669.125 s. The time allowing the propagation of an ultrasonic wave from emitter to receiver in the cavity (t) was calculated for different vol. % of H₂. For H₂ = 0%, the value obtained is 669.125 s which reduces by 3.12 s with every 1% vol. % increase of H₂ w.r.t air.

For calibrating the sensor device, a

fixed H₂ concentration (2%) (verified by ultrasonic transducer) was made to flow into the testing set-up and the voltage on the monitor was adjusted to ensure 1:1 relation with the gas concentration. The sensor response was then recorded for the entire range of H₂ conc. from 0-3.5% at an interval of 0.5%. Fig. 6(a) depicts the sensor response (black) in volts at various time of flight values. The data is

superimposed with actual calculated H₂ conc. (red) flowing in the dynamic set-up. As clearly shown, sensor response agrees well with the calculated values with displayed voltage values (y-axis) directly related to H₂ conc. The same can be transformed into a calibration curve.

As seen in Fig. 6(b), the sensor response varies linearly as a function of H₂

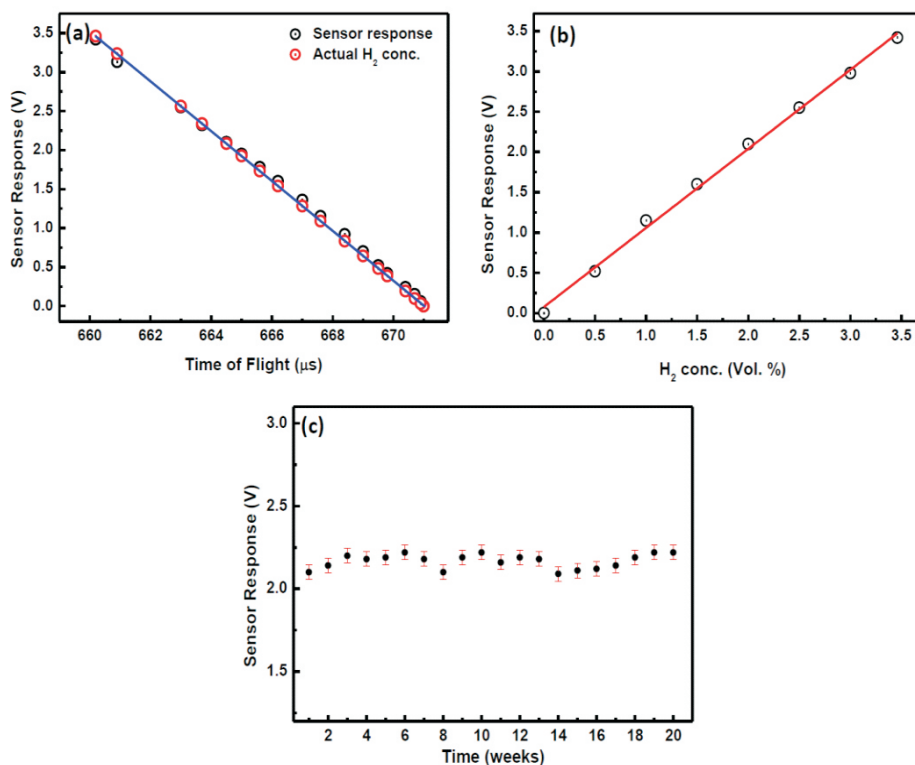


Fig. 6: (a) sensor response as a function of time of flight in ultrasonic transducer, superimposed on calculated H₂ concentration values, (b) Calibration curve derived from time of flight data, and (c) Sensor response at fixed H₂ concentration of 2% as a function time.

Measuring Range	0.3 – 4.0% in air
Operating Temperature	150 °C
Response Time	2-5 sec
Recovery Time	2-3 min
Sensitivity	0.3 %
Working Lifespan	> 3 year
Noise Level	± 100 mV

Table 1. Technical Specifications of H₂ sensor

concentration tested up to 3.5%. Fig. 6(c) shows the repeatability/stability data recorded for subsequent weeks for 2% H₂ concentration with error bars as a measure of standard deviation. The technical specifications of the sensor device are listed in Table 1.

Conclusion

We have successfully developed Pd-thin film based Pellister type H₂ sensor at Technical Physics Division, BARC. The sensor device has been designed in-house, fabricated, tested using an in-house made dynamic gas sensing set up. The sensor device exhibits linear sensor response in presence of H₂ gas (0-3.5% conc.) with a minimum detection limit of 0.3%. The calibration of sensors is carried out using ultrasonic transducer to ensure high precision. 90% of the sensor films exhibit a life-time > 3 years. Till date we supplied 16 sensor devices to various users within and outside DAE.

Acknowledgements

Authors are thankful to Dr. T. V. Chandrasekhar Rao, Head, Technical Physics Division and Shri Sanjay Malhotra, Head, Electromagnetic Application & Instrumentation Division for their support in this development. Authors also express gratitude to Dr. S.K. Gupta & Dr. S.C. Gadkari Former Heads, Technical Physics Division, Shri V.R. Katti and Shri J.C. Vyas for their encouragement in this work.

Corresponding Author*

Niyanta Datta (niyanta@barc.gov.in)

References

[1] A. K. Basu, S. Tatiya, G. Bhatt, S. Bhattacharya. "Fabrication processes for sensors for automotive applications: a review". Sensors Automot Aersp Appl, Singapore, Springer, 2019.

- [2] M.N. Carcassi, F. Fineschi. "Deflagrations of H₂-air and CH₄-air lean mixtures in a vented multi-compartment environment". Energy, 30 (2005): **1439-1451**.
- [3] Sadullah Oztürk, Necmettin Kılınc. "Pd thin films on flexible substrate for hydrogen sensor". Journal of Alloys and Compounds, 674 (2016): **179-184**.
- [4] Xiaoyi She, Yang Shen, Jianfang Wang and Chongjun Jin. "Pd films on soft substrates: a visual, high-contrast and low-cost optical hydrogen sensor". Light: Science & Applications, 8 (2019): **4**.
- [5] D.W. Dabill, S.J. Gentry, P.T. Walsh. "A fast-response catalytic sensor for flammable gases". Sensors & Actuators, 11 (1987): **135-143**.
- [6] P.T. Moseley, B.C. Tofield (Eds). Solid State Gas Sensors. Bristol, UK, IOP Publishing Ltd., Adam Hilger, 1987.
- [7] Young Tack Lee, Jun Min Lee, Yeon Ju Kim, Jin Hyoun Joe and Wooyoung Lee. "Hydrogen gas sensing properties of PdO thin films with nano-sized cracks". Nanotechnology, 21(2010): **165503**.
- [8] Sylwia Owczarek, Sten V. Lambeets, Robert Bryl, Cédric Barroo, Olivier Croquet, Leszek Markowski & Thierry Visart de Bocarmé. "Oxygen Adsorption, Subsurface Oxygen Layer Formation and Reaction with Hydrogen on Surfaces of a Pt-Rh Alloy Nanocrystal". Topics in Catalysis, 63 (2020): **1522-1531**.

Structural Behaviour of Superconducting H₃S at Megabar Pressure

P. Modak* and A. K. Verma

High Pressure & Synchrotron Radiation Physics Division
Bhabha Atomic Research Centre, Mumbai-400085, India

Abstract

A new era has begun in the field of superconductivity with the discovery of phonon mediated superconductivity at 203 K in the compressed hydrogen disulfide (H₂S) gas. A series of studies has attributed the observed superconductivity to a compound H₃S that results from the decomposition of compressed H₂S at high pressures. The superconducting properties of conventional superconductors can be computed precisely once the underlying microscopic crystal structure is fully known. In this work using evolutionary crystal structure searches in combination with first-principles calculations, we predict a new metallic phase of H₃S in the pressure interval of 108-166 GPa. The novelty of new phase is that it consists of SH₆, SH₃ and S units that results both cationic and anionic charge state for S and H atoms. Our work shows that the high-T_c explanations based on structures reported earlier may not be adequate and thus more work is needed for arriving at a precise understanding of the observed high-T_c in this material.

Keywords: Phonon mediated superconductivity, Metallic phase, crystal orbital Hamiltonian population (COHP)

Introduction

Superconductivity the phenomenon of non-resistive conduction of electricity below critical temperature (T_c) remains one of the hot topics in the material science. It was first discovered by H. K. Onnes in Hg at 4.2 K in 1911. Over the years several new superconductors were identified leading to the discovery of 18 K superconductivity in Nb₃Sn in 1954 [1]. However, the ultimate goal of achieving a room temperature superconductor is still a distant dream though a T_c of 133 K has been achieved in the Hg based cuprates at ambient pressure that increases to 164 K at 30 GPa [2, 3]. The prospect of getting higher T_c in this family of compounds is not clear as the nature of superconductivity is still not fully understood. In contrast, the Bardeen-Cooper-Schrieffer (BCS) formalism provides a clear guide to achieve high T_c; all that needed is a favourable combination of high frequency phonons, strong electron-phonon coupling and high electronic density of states at the Fermi level. Based on the BCS formalism, it was predicted that under the application of pressures of the order of 25 GPa, Hydrogen would exhibit superconductivity at high

temperature [4, 5]. However the metallization of hydrogen is a challenging problem in the high pressure research to date. Formation of metallic atomic hydrogen at high pressure has been difficult to establish in diamond-anvil cells. There have been claims on experimental evidence for a metallic phase at pressures,

from 250 GPa to 495 GPa [6-8], but the findings of these works have not yet been unambiguously accepted by the scientific community [6-10]. Ashcroft [11] proposed that the metallization pressure for hydrogen could be lowered by chemical pre-compression or via doping. Driven by this idea, there is a surge in the high pressure research activities on the hydrogen rich solids in recent years [12-14].

One of the remarkable successes of these efforts is the observation of a record breaking 203 K superconductivity in the compressed H₂S gas announced in the year 2015 [15]. Though the T_c is well below the room temperature, this discovery is considered to be a definitive forward step towards the realisation of a room temperature superconductor. However the composition and crystal structure of superconducting phase have not been well characterized, as it is observed that compressed H₂S molecules dissociate under high pressure (above 27 GPa and at 300 K) [16]. A large number of

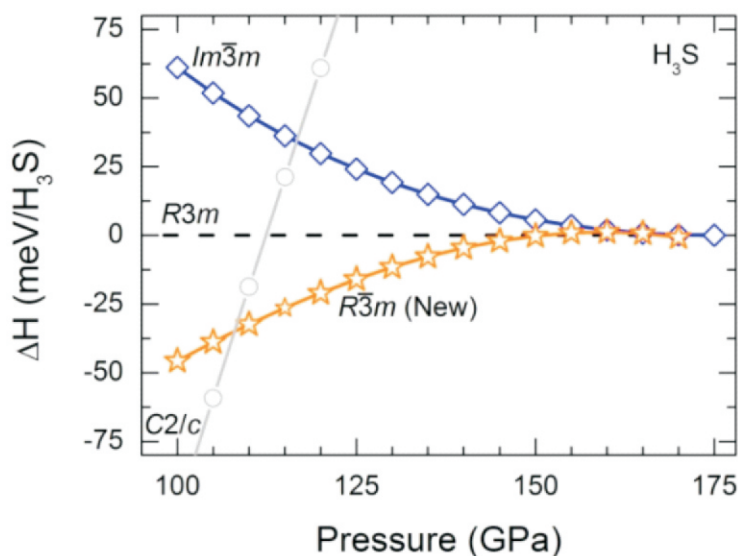


Fig. 1: Pressure variation of enthalpy for the most important structures of H₃S. Here enthalpies are estimated relative to known *R*3*m* structure (Ref. 23).

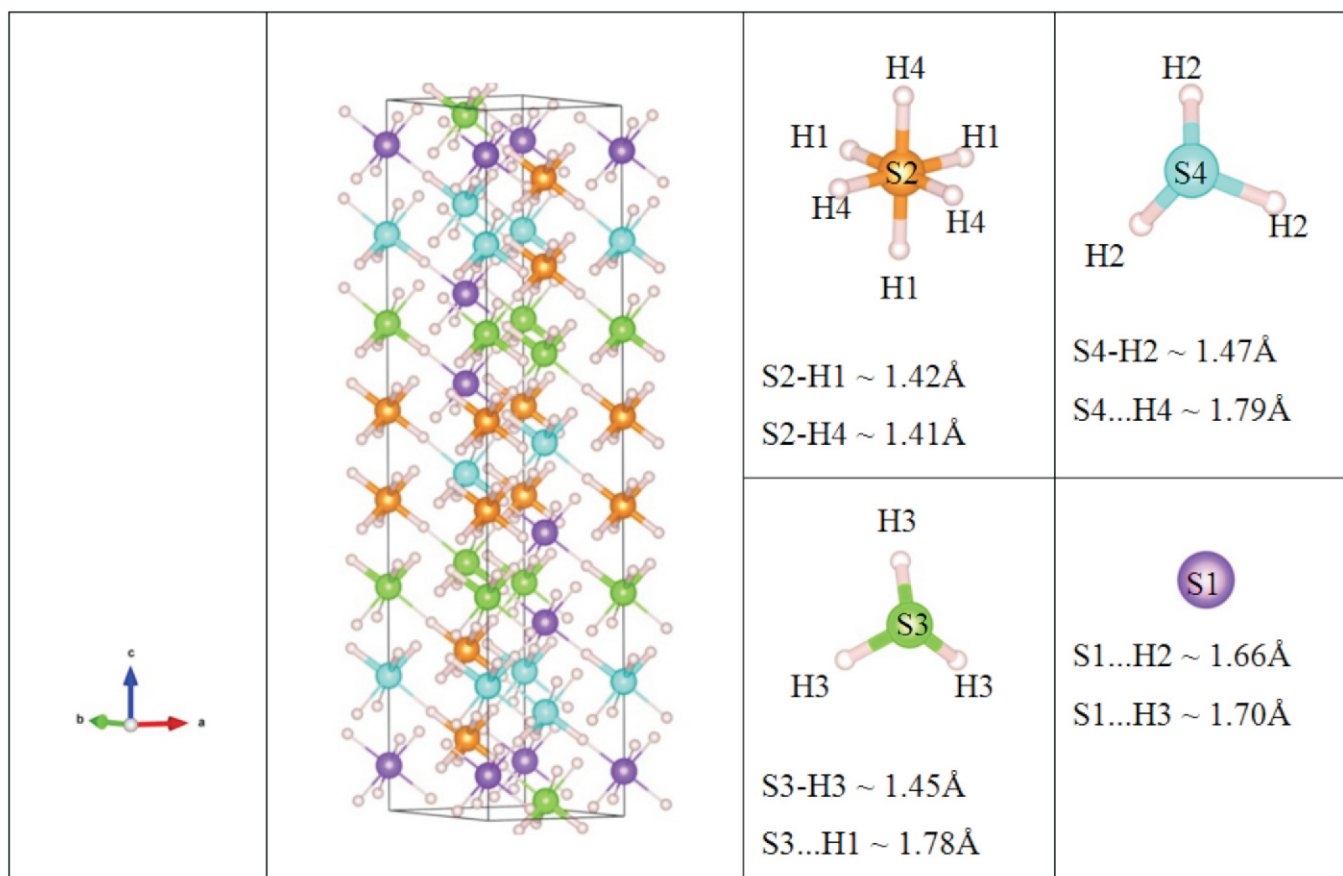


Fig. 2: Ball-and-stick model of the newly predicted trigonal structure ($R\bar{3}m$, $Z=24$) of H_3S . Here, S-H covalent bonds are shown by thick rods and S...H hydrogen bonds are shown by thin rods. Bond-lengths are given at 110 GPa (Ref. 23).

investigations, on the high pressure behaviour of H-S system, have commenced immediately after this discovery [17-19]. A consensus about decomposition of H_2S and formation of new compounds under high pressure emerged based on consistent results reported from several experimental and theoretical studies [18-19]. It is widely believed that the formation of H_3S compound is responsible for the high T_c superconductivity in compressed H_2S . Recent high pressure experiments with H_2+S sample reports formation of H_3S compound above 70 GPa [20].

There are reports on the high pressure phase diagram of H_3S compound based on first principle studies [17, 21]. It is predicted that H_3S metalizes at 112 GPa in trigonal structure ($R\bar{3}m$, $Z=3$); further compression would result in a phase transition to cubic bcc structure ($Im\bar{3}m$, $Z=2$) around 175 GPa [17]. Few other non-metallic H_3S structures, orthorhombic ($Cccm$, $Z = 16$, 37-112 GPa), monoclinic ($C2/c$, $Z = 16$, 2-112 GPa) and triclinic $P1$ ($Z=8$, 0-37 GPa), were also proposed. Surprisingly lowest enthalpy non-metallic $C2/c$ structure has not been observed in

any experiments but they observed orthorhombic $Cccm$ structure [20, 22]. Hence the high pressure phase diagram of H_3S is still not well characterized even after various theoretical and experimental studies. Recently, we have carried out high pressure crystal structure searches using evolutionary algorithm combining with first-principles relaxations to unveil the high pressure phase diagram of H_3S [23]. Results are discussed in the light of the experimentally observed pressure dependence of the transition temperature T_c .

Theoretical methods

Crystal structure searches were carried out using evolutionary algorithm as implemented in the USPEX code [24-26] and the first-principles calculations were carried out using VASP code [27-30]. In these calculations, we have used all-electron frozen-core projector-augmented wave (PAW) potentials and generalized-gradient approximation (GGA) for exchange-correlation energy. To understand bonding characteristics we have also calculated crystal orbital Hamiltonian population (COHP) using

TB-LMTO-ASA code [31].

Results & Discussion

In low pressure region (<100 GPa) our crystal structure searches correctly reproduce all earlier known structures. Below 108 GPa, we find a monoclinic structure ($C2/c$, $Z = 16$) as the energetically most favourable structure. We also predict two new metastable structures namely; a monoclinic ($C2/m$, $Z = 16$) and a tetragonal structure ($P4\bar{c}2$, $Z = 8$) in this pressure region. We find that our proposed tetragonal $P4\bar{c}2$ structure is energetically superior to the earlier proposed orthorhombic structure ($Cccm$, $Z = 16$). Further we noticed that orthorhombic $Cccm$ structure relaxes to tetragonal $P4\bar{c}2$ structure under full structural optimization at 75 GPa and above. Although $C2/m$ and $P4\bar{c}2$ structures do not have the lowest enthalpies but the possibility of their formation is not completely ruled out under favourable conditions of pressure and temperature.

Above 100 GPa our searches uncover a completely new trigonal structure ($R\bar{3}m$, $Z=24$) which is energetically superior to the earlier accepted trigonal

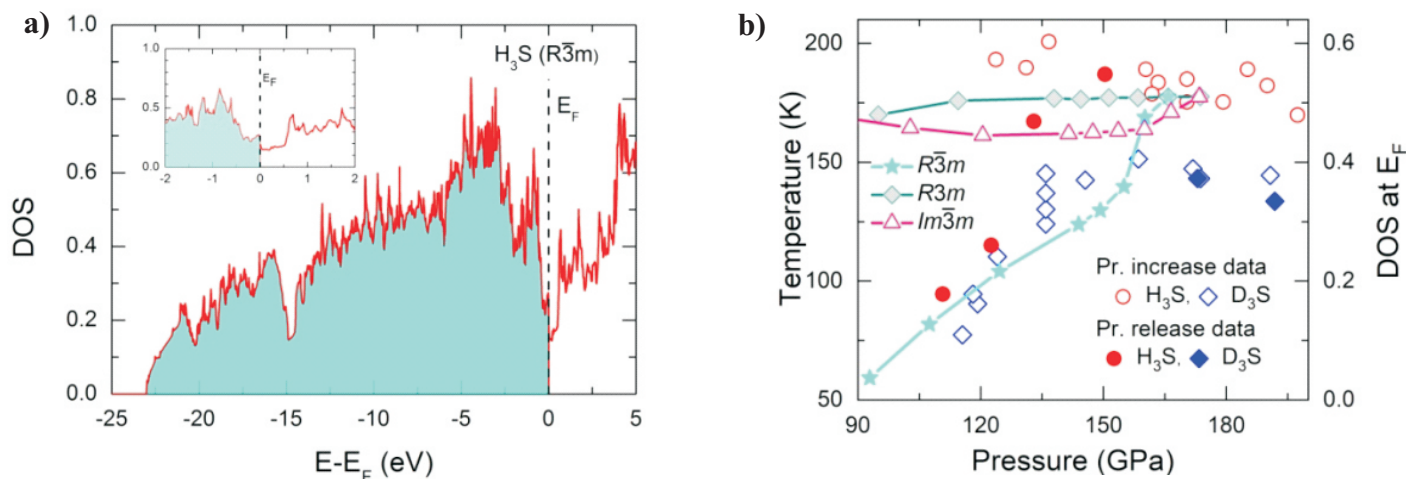


Fig. 3: (a) Total Electronic DOS of $R\bar{3}m$ phase of H_3S at 120 GPa. (b) Pressure variation of total DOS value at the Fermi-level. Here DOS is given in units of states/eV/ H_3S . (Ref. 23).

structure ($R3m$, $Z=3$). We find that the low pressure monoclinic $C2/c$ structure makes a transition to our new structure at 108 GPa with a 6.25% volume reduction. On further compression $R\bar{3}m$ structure transforms to a cubic structure ($Im\bar{3}m$, $Z=2$) at 166 GPa. Therefore the stability region of $R\bar{3}m$ structure is 108-166 GPa (Fig.1). We also find that in the pressure range 150-166 GPa two trigonal structures coexist with very small differences in enthalpy (maximum enthalpies difference ~ 1.0 meV/ H_3S). The dynamic stability of this new structure is established by calculating phonon spectrum that contains only real and positive frequencies.

Now to understand to what extent this newly found $R\bar{3}m$ structure differs from earlier known $R3m$ and $Im\bar{3}m$ structures we carried out its structural analysis. We find that the new structure consists of SH_6 , SH_3 and S units contrary to the $R3m$ and $Im\bar{3}m$ structures that consist of only SH_3 and SH_6 , respectively (Fig. 2). In all three structures the structural units are connected through S...H hydrogen-bonds. Presence of different structural units in the new structure leads to different local environments around S atoms that in turn results four different bond lengths both for S-H covalent and S...H hydrogen-bonds (Fig.2).

Our Bader charge analysis reveals different charge states for S and H atoms in different structural units of this structure. We find SH_6 unit is very similar to SF_6 molecule as in both units S has positive charge and H has negative charge like halide ions. But in the SH_3 unit S has negative charge and H has

positive charge like alkali ions. Therefore both cationic and anionic charge states of H and S exist in new structure. We find that in $R\bar{3}m$ structure pressure induced symmetrization of hydrogen-bonds take place at, ~ 166 GPa where it makes a transition to a cubic $Im\bar{3}m$ structure.

Our electronic structure analysis shows that three electronic bands cross the Fermi-level leading to one hole and two electron Fermi-sheets for new structure. We find that the total electronic DOS function is free electron like below to -20 eV, however close to the Fermi-level, on occupied side, there is a peak corresponding to van Hove singularity (VHS) and on other side there is a pseudo gap (Fig.3a). The van Hove singularity represents a critical point in the electronic density of state (DOS) function which induces electronic instabilities in the system. Generally, it has been seen that a VHS helps in formation of lower energy states like superconductivity. Pseudogap refers to a minimum in the electronic DOS function at the Fermi-level but in the context of superconductivity, especially in high-temperature superconductors; it refers to an energy range near the Fermi level which has very few states associated with it. Generally, pseudogaps forms when favourable electron-lattice interactions are present in the system. Underdoped cuprate superconductors are famous examples that exhibit pseudogaps above the transition temperature.

We find that close to the Fermi-level the DOS contributions come mainly from hydrogen $1s$ and sulfur $3p$ states. The S

atom present in SH_6 structural unit contributes maximum to the DOS value at the Fermi-level. Compared to the old $R3m$ structure, the total DOS value at Fermi-level for $R\bar{3}m$ structure is considerably lower and it smoothly increases under pressure reaching to that of $Im\bar{3}m$ structure near to 166 GPa. As electron-phonon coupling constant is directly proportional to DOS value at the Fermi-level, we expect lower electron-phonon coupling and consequently the lower T_c for $R\bar{3}m$ structure below 155 GPa provided other parameters remain unaltered. Interestingly the pressure variation of DOS value at the Fermi-level behaves similar to the observed pressure variation of T_c (Fig.3b). It is worth mentioning that the Fermi-level DOS values of the earlier structures (i.e., $R3m$ and $Im\bar{3}m$) do not exhibit such pressure behaviour, their Fermi-level DOS values remain nearly constant under pressure and hence they do not support the experimental observations.

Mechanism of superconductivity in compressed H_3S is widely believed to be of BCS type and the observation of strong isotope shift of T_c in deuterated samples further supports this view [15, 32]. The experimental value of the isotope coefficient (α) is ~ 0.3 , at pressure above 170 GPa [15]. It is worthwhile to mention that the ideal BCS value of is 0.5. However deviations in α values, from the 0.50, are a general feature of the BCS type superconductors. In recent years proposals of a non-BCS type of mechanism in H_3S are also put forward by some groups of researchers [33-35].

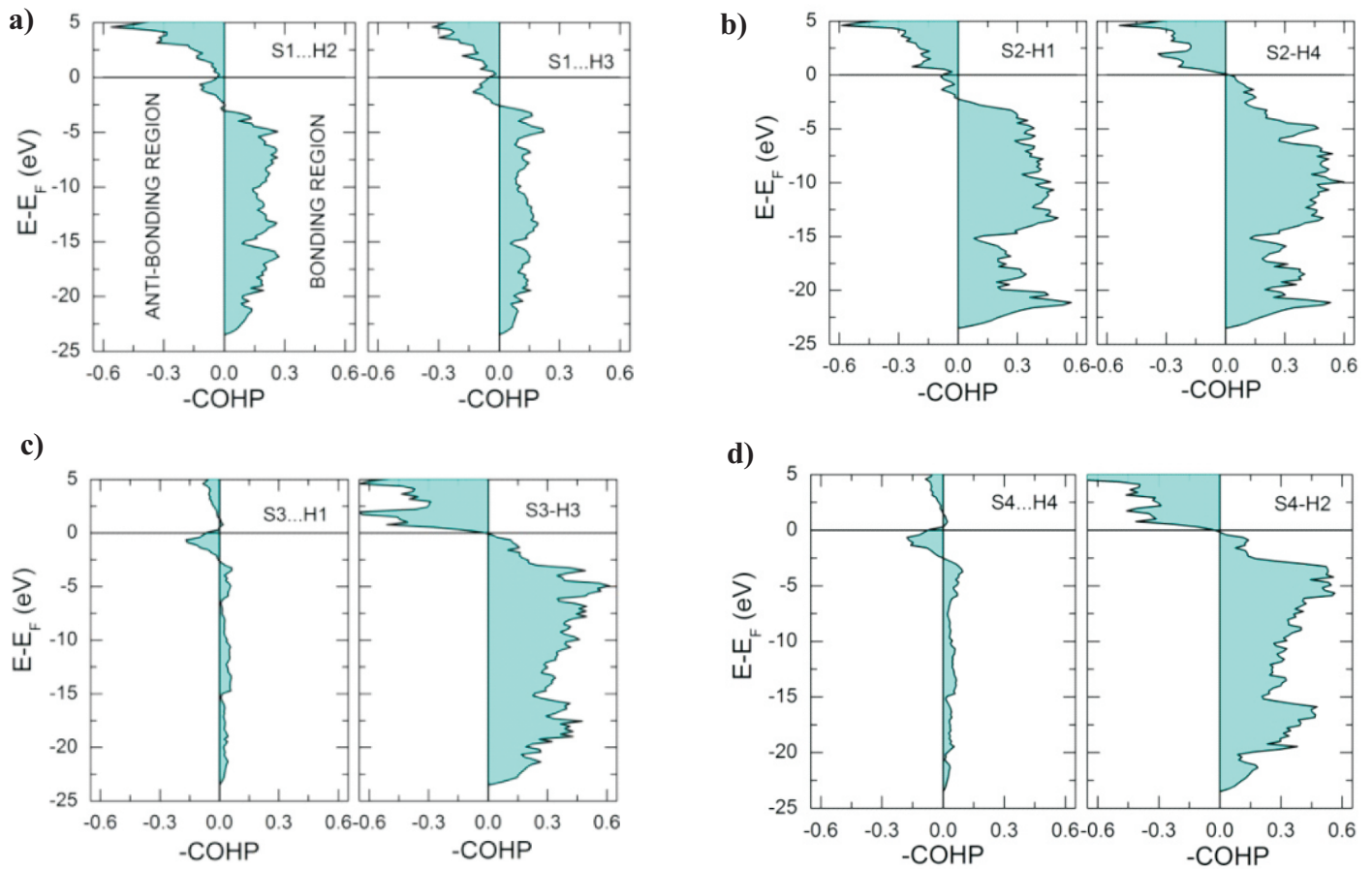


Fig. 4: The COHP functions of $R\bar{3}m$ phase of H_3S at 120 GPa (Ref.23).

To understand the nature of S-H covalent bonds in different structural units, we have carried out crystal orbital Hamiltonian populations (COHP) analysis [36]. The COHP is an efficient tool to extract bonding information based on the electronic structure calculations. In a given energy window, its negative values describe bonding interactions and positive values describe anti-bonding interactions. It is customary to plot $-COHP$ as a function of energy as shown in Fig.4 for different S-H pairs. Our analysis show that except S2-H1 covalent bond all other covalent bonds give bonding interactions as COHP is negative below Fermi-level. For $R\bar{3}m$ and $Im\bar{3}m$ structures, we find that the Fermi-level is located in the region of anti bonding states for S-H covalent bonds indicating an inherent instable nature of these structures. This also explains why $R\bar{3}m$ structure is more stable compared to $R\bar{3}m$ and $Im\bar{3}m$ structures. We also find that S...H hydrogen bonds around S structural units have significant covalent character. COHP analysis also reveals that the S-H and B-B covalent bonds in MgB_2 are different in character as the origin of metallicity of these two bonds is different.

Conclusions

In summary, we have studied the structural behaviour of H_3S under high pressure using evolutionary crystal structure searches and first-principles calculations. Our searches unveiled a completely new structure in the trigonal crystal system over a large pressure interval (~ 108 -166 GPa). The newly proposed structure is metallic in nature and it consists of SH_6 , SH_3 and S units that are connected through strong S...H hydrogen-bonds. In the SH_6 unit, H is chemically halogen like whereas in SH_3 units it behaves like alkali metal. At lower pressures new structure has smaller total electronic DOS at Fermi level in comparison to earlier structures hinting that earlier T_c estimations based on old structures may not be precise. Interestingly, for new structure pressure variation of total DOS values at the Fermi-level correlate well with the observed pressure variation of superconducting transition temperature that is absent for the earlier $R\bar{3}m$ structure.

Corresponding Author*

P Modak (pmodak@barc.gov.in)

References

- [1] B. Matthias, T. Geballe, S. Geller, and E. Corenzwit, Phys. Rev., **95**, 1435 (1954).
- [2] A. Schilling, M. Cantoni, J. D. Guo and H. R. Ott, Nature, **363**, 56 (1993).
- [3] L. Gao, Y. Y. Xue, F. Chen, Q. Xiong, R. L. Meng, D. Ramirez, C. W. Chu, J. H. Eggert, and H. K. Mao, Phys. Rev. B, **50**, 4260 (1994).
- [4] E. Wigner, and H. B. Huntington, J. Chem. Phys., **3**, 764–770 (1935).
- [5] N. W. Ashcroft, Phys. Rev. Lett., **21**, 1748–1749 (1968).
- [6] P. Loubeyre, F. Occelli and P. Dumas, Nature, **577**, 631 (2020).
- [7] M. Eremets, I. Troyan and A. P. Drozdov, arXiv: Materials Science (2016).
- [8] R. P. Dias and I. F. Silvera, Science, **355**, 715 (2017).

- [9] X.-D. Liu, P. Dalladay-Simpson, R.T. Howie, B. Li, and E. Gregoryanz, *Science*, **357**, eaan 2286 (2017).
- [10] A.F. Goncharov and V.V. Struzhkin, *Science*, **357**, eaan9736 (2017).
- [11] N. W. Ashcroft, *Phys. Rev. Lett.*, **92**, 187002 (2004).
- [12] M. Somayazulu, M. Ahart, A. K. Mishra, Z. M. Geballe, M. Baldini, Y. Meng, V.V. Struzhkin, and R. J. Hemley, *Phys. Rev. Lett.*, **122**, 027001 (2019).
- [13] A. P. Drozdov, P. P. Kong, V. S. Minkov, S. P. Besedin, M. A. Kuzovnikov, S. Moza_ari, L. Balicas, F. Balakirev, D. Graf, V. B. Prakapenka, E. Greenberg, D. A. Knyazev, M. Tkacz, and M. I. Eremets, *Nature*, **569**, 528 (2019).
- [14] E. Snider, N. Dasenbrock-Gammon, R. McBride, M. Debessai, H. Vindana, K. Vencatasamy, K. V. Lawler, A. Salamat, and R. P. Dias, *Nature*, **586**, 373 (2020).
- [15] A. P. Drozdov, M. I. Eremets, I. A. Troyan, V. Ksenofontov, and S. I. Shylin, *Nature*, **525**, 73 (2015).
- [16] H. Fujihisa, H. Yamawaki, M. Sakashita, A. Nakayama, T. Yamada, and K. Aoki, *Phys. Rev. B*, **69**, 214102 (2004).
- [17] D. Duan, Y. Liu, F. Tian, D. Li, X. Huang, Z. Zhao, H. Yu, B. Liu, W. Tian, and T. Cui, *Sci. Rep.*, **4**, 6968 (2014).
- [18] N. Bernstein, C. S. Hellberg, M. D. Johannes, I. I. Mazin, and M. J. Mehl, *Phys. Rev. B*, **91**, 060511(R) (2015).
- [19] I. Errea, M. Calandra, C. J. Pickard, J. Nelson, R. J. Needs, Y. Li, H. Liu, Y. Zhang, Y. Ma, and F. Mauri, *Phys. Rev. Lett.*, **114**, 157004 (2015).
- [20] B. Guigue, A. Marizy and P. Loubeyre, *Phys. Rev. B*, **95**, 202104 (2017).
- [21] Y. Li, L. Wang, H. Liu, Y. Zhang, J. Hao, C. J. Pickard, J. R. Nelson, R. J. Needs, W. Li, Y. Huang, I. Errea, M. Calandra, F. Mauri, and Y. Ma, *Phys. Rev. B*, **93**, 020103(R) (2016).
- [22] A. F. Goncharov, S. S. Lobanov, I. Kruglov, X. M. Zhao, X. J. Chen, A. R. Oganov, Z. Konopkova and V. B. Prakapenka, *Phys. Rev. B*, **93**, 174105 (2016)
- [23] Ashok K. Verma and P. Modak, *Phys. Chem. Chem. Phys.*, **20**, 26344 (2018).
- [24] A.R. Oganov and C.W. Glass, *J. Chem. Phys.*, **124**, 244704 (2006).
- [25] A. O. Lyakhov, A.R. Oganov, H.T. Stokes, and Q. Zhu, *Comp. Phys. Comm.*, **184**, 1172 (2013).
- [26] A.R. Oganov, A.O. Lyakhov, and M. Valle, *Accounts of Chem. Research*, **44**, 227 (2011).
- [27] G. Kresse and J. Hafner, *J. Phys.: Condens. Matter*, **6**, 8245 (1994).
- [28] P. E. Blöchl, *Phys. Rev. B*, **50**, 17953 (1994).
- [29] G. Kresse, and J. Furthmuller, *Comput. Mater. Sci.*, **6**, 15 (1996).
- [30] G. Kresse, and D. Joubert, *Phys. Rev. B*, **59**, 1758 (1999).
- [31] O. K. Andersen, Stuttgart Tight-binding LMTO Program version 4.7, *Max Planck Institute Für Festkörperforschung*.
- [32] I. A. Troyan, et al., *Science* **351**, 1303–1306 (2016).
- [33] N. Bernstein, C. S. Hellberg, M. D. Johannes, I. I. Mazin, M. J. Mehl, *Phys. Rev. B* **91**, 060511 (2015).
- [34] S. Mozaffari et al., *Nature Communications* **10**, 2522 (2019).
- [35] E. F. Talantsev, *Supercond. Sci. Technol.* **33**, 124001 (2020).
- [36] R. Dronskowski, and P. E. Blöchl, *J. Phys. Chem.*, **97**, 8617 (1993).

This page is intentionally left blank



Dhruva Reactor

Edited & Published by:
Scientific Information Resource Division
Bhabha Atomic Research Centre, Trombay, Mumbai 400 085, India
BARC Newsletter is also available at URL:<http://www.barc.gov.in>